

DESY SR-75/17
October 1975

DESY-Bibliothek
15. DEZ. 1975

Exciton Dynamics in Solid Neon

by

D. Pudewill

II. Institut für Experimentalphysik der Universität Hamburg

F.-J. Himpsel, V. Saile, N. Schwentner and M. Skibowski
Sektion Physik der Universität München

E. E. Koch

Deutsches Elektronen-Synchrotron DESY, Hamburg

Joshua Jortner

*Department of Chemistry,
Tel-Aviv University,
Tel-Aviv, Israel*

To be sure that your preprints are promptly included in the
HIGH ENERGY PHYSICS INDEX ,
send them to the following address (if possible by air mail) :

DESY
Bibliothek
2 Hamburg 52
Notkestieg 1
Germany

Exciton Dynamics in Solid Neon[†]

D. Pudewill

II. Institut für Experimentalphysik der Universität Hamburg, Germany

F.-J. Himpsel, V. Saile, N. Schwentner⁺ and M. Skibowski⁺⁺

Sektion Physik der Universität München, München, Germany

a n d

E.E. Koch

Deutsches Elektronen-Synchrotron DESY, Hamburg, Germany

a n d

Joshua Jortner[§]

Department of Chemistry, Tel-Aviv University, Tel-Aviv, Israel

[†] Work supported in part bei Deutsche Forschungsgemeinschaft DFG and Bundesministerium für Forschung und Technologie BMFT and by the Nerken Foundation at the University of Tel-Aviv.

⁺ Now at Christian Albrechts University, Kiel, Germany.

⁺⁺ On leave at Xerox, Palo Alto Research Center, Palo Alto, California, and University of Illinois, Urbana-Champaign, Illinois, USA.

[§] On leave at Dept. of Chemistry University of California at Berkeley, California, USA.

ABSTRACT

In this paper we report the results of an experimental study of the photoelectric yield of pure and doped solid Ne in the extreme ultraviolet ($\hbar\omega = 8-30$ eV) by use of synchrotron radiation from the DESY-synchrotron. Results for the range of impurity excitations, exciton states and inter-band transitions were obtained for Xe in Ne, Kr in Ne and Ar in Ne. The photoemission data were utilized to extract new information concerning

- (a) energetics
- (b) non radiative relaxation phenomena and
- (c) exciton dynamics in solid Ne.

Concerning (a) a definite value for the electron affinity V_0 in solid Ne was established experimentally. Concerning (b) we were able to show that the $n = 2$ ($1/2$) exciton state decays in an Auger type process into an ionized impurity in the $3/2$ state and a free electron on a time scale τ (Auger) $\leq 10^{-13}$ sec, which is comparable or even shorter than the $n = 2 \rightarrow n = 1$ nonradiative relaxation process. Concerning (c) the analysis of the energy dependent photoemission line shape at different film thicknesses resulted in information concerning the diffusion length of excitons and escape length of electrons in solid Ne.

1. INTRODUCTORY COMMENTA

There have been extensive experimental and theoretical studies aimed towards a complete understanding of the electronic states of solid rare gases and their dilute alloys, which provide a prototype of simple molecular crystals, characterized by a large band gap^{1}. These investigations fall into three different categories. First, static features of the valence and conduction band states and of exciton states were probed by optical absorption and reflection spectroscopy^{2}, by photoemission yield studies^{3-5} and by measurements of the energy distribution of photoelectrons (EDC's)^{10-12}. Second, some information concerning non-radiative relaxation phenomena in pure and doped systems was gathered from optical emission studies as well as from photoemission data^{13}. Third, the dynamics of exciton states in solid rare gases were recently monitored by photoemission studies^{8}.

Regarding the electronic states of solid rare gases and their dilute alloys the following information emerges:

- (a) The width of the valence band is 1.3 eV in solid Ne, 1.7 eV in solid Ar, 2.3 eV in solid Kr and 3.0 eV in solid Xe^{11}.
- (b) The conduction band is parabolic, its widths being quite well approximated by the nearly-free-electron formula $W_c \approx h^2/2ma^2$, where m is the bare electron mass and a is the lattice constant.
- (c) Exciton states located below the direct threshold for interband transitions are exhibited both in pure solid rare gases and in their dilute alloys^{11,14-16}. The energies $E_n(j)$ of high excitons with principal quantum number $n \geq 2$ and the energies $E_n^i(j)$ of excited impurity states can be described in terms of a Wannier series converging to the bottom of the conduction band

$$E_n(j) = E_G(j) - B/n^2$$

$$E_n^i(j) = E_G^i(j) - B^i/n^2$$
(1)

where $E_G(j)$ and $E_G^i(j)$ are the interband gap in the pure solid and the impurity energy gap, respectively, while B and B^i correspond to the effective Rydberg constants for the exciton and for the impurity states, respectively. The total angular momentum quantum number of the hole can take the values $j = 3/2$ and $j = 1/2$, so that in solid Ar, Kr and Xe and for the impurity states of these elements two Wannier series split by spin orbit coupling are exhibited. Eq. (1) is applicable for $n > 2$ while for the lowest $n = 1$ state large central cell corrections, within the framework of the Wannier scheme, have to be incorporated. The values of all the energy parameters in eq. (1) for all solid rare gases and for dilute impurity states in these solids are now well established.

(d) The effective-mass, m^f , of the electron in the conduction band in solid Ne, Ar, Kr and Xe as inferred from the experimental B^i values is $m^f = 0.4 - 0.6$, reflecting the effects of short range electron-atom repulsions.

(e) The energy V_o ($\equiv -E_A$) of the bottom of the conduction band relative to the vacuum level was deduced from intrinsic photoemission yield studies and from EDC data, which result in the threshold energies E_{TH} for the pure solid and E_{TH}^i for the impurity state, whereupon

$$V_o = E_G(3/2) - E_{TH}$$

$$V_o = E_G^i(3/2) - E_{TH}^i$$
(2)

From the combination of optical absorption data for $E_G(3/2)$ and $E_G^i(3/2)$ and of photoemission data the following data were obtained:

$V_o = + 0.3 \pm 0.1$ eV for solid Ar, $V_o = - 0.3 \pm 0.1$ eV for solid Kr and $V_o = - 0.45 \pm 0.05$ eV for solid Xe, while recent EDC data yield $V_o \approx + 1.4$ eV for solid Ne^{4,8,11}.

The following qualitative information is currently available from energy resolved (rather than time resolved) studies of nonradiative relaxation phenomena in pure and doped solid rare gases^{13}.

(f) Exciton trapping in solid Ar, Kr and Xe. The vacuum ultraviolet emission spectra of pure solid Ar, Kr and Xe and of impurity pairs of Ar, Kr and Xe in Ne, Ar, Kr and Xe host crystal excited by an α -source, X-rays, electron beams and by optical sources exhibit the emission from electronically excited, vibrationally relaxed, rare-gas homonuclear diatomics. No optical emission was detected from "free" exciton states, so we can conclude that efficient exciton trapping, via vibrational relaxation occurs in these solids in a time scale τ_t , which is short relative to the radiative lifetime τ_r , i.e. $\tau_t \leq 10^{-2} \tau_r$ and as $\tau_r \sim 10^{-9}$ sec, $\tau_t \leq 10^{-11}$ sec. The trapped exciton in solid Ar, Kr and Xe is practically immobile due to small polaron effects.

(g) Emission from "free" excitons in solid Ne. The optical emission of solid Ne at 6 K exhibits the radiative decay of a "phonon dressed" free exciton^{17}. In this solid exciton trapping via the formation of a diatomic molecule does not take place due to an inefficient vibrational relaxation (on the time scale of τ_r) whereupon $\tau_t \gg \tau_r$.

(h) Non radiative relaxation from high exciton states. In pure solid Ne, Ar, Kr and Xe as well as for impurity states the optical emission spectra are independent of the excitation energy. Thus the non radiative relaxation τ_{nr} from high exciton states $n > 1$ to the lowest $n = 1$ (3/2) state is fast in the time scale of the radiative decay of these states, i.e. $\tau_{nr} < 10^{-11}$ sec or so.

These experimental observations are borne out by theoretical calculations^{13,28}.

(i) Electron-electron scattering. The onset of electron-electron scattering originating from exciton-pair production was observed^{4} in photo-emission studies of Ar, Kr and Xe at energies close to $E_E + E_1$ (3/2).

Studies of exciton dynamics in solid rare gases are of much more recent vintage. The diffusion lengths of "free" (i.e. phonon dressed) excitons in solid Ar and Xe were experimentally determined by two independent techniques which rest on photoemission yield studies: (1) The Auger-type exciton enhanced impurity photoemission method was explored^{7,8} and (2) extrinsic photoemission data from pure solid Xe deposited on a gold substrate at excitation energies below E_{TH} resulting from energy transfer from mobile excitons to the metal substrate was utilized^{18}. These studies resulted in:

- (j) The diffusion length of "free" excitons in the heavier pure solid rare gases are $\sim 120 \text{ \AA}$ for solid Ar at 20° K and $\sim 300 \text{ \AA}$ for solid Xe at 40 K . These large diffusion lengths are quite remarkable in view of the short lifetimes of "free" excitons in these solids (point (f)).
- (k) Exciton scattering occurs at each site and the "free" exciton motion is diffusive rather than coherent. This expectation is borne out by estimates of the mean free path for the scattering of $n = 1$ ($3/2$) Wannier excitons in solid Ar and Xe which is comparable to the lattice spacing^{7,8}.

The wealth of information currently available for the energetics, relaxation phenomena and exciton dynamics in solid rare gases reveals one glaring gap, which pertains to the nature of exciton dynamics in solid Ne. The absorption spectrum of pure solid Ne¹⁶, reproduced in Fig. 1, spans the energy range above 17 eV. It reveals a single Wannier series, a reasonable result in view of the small spin-orbit splitting of 0.10 eV in the gasphase, which is comparable to the line widths in optical absorption. The optical spectra of dilute impurity states of Ar, Kr and Xe in solid Ne which were recently studied^{16} spanning the energy range 9-17 eV exhibit long Wannier series providing the first reliable set of E_G and E_G^i values for this solid. In view of the absence of exciton trapping in solid Ne (point (g)) the gross features of energy transfer via "free" exciton states in this solid should be drastically different from the quantitative features of exciton dynamics in solid Ar, Kr and Xe. To be more specific, we expect that in view of the long $\tau_o \approx \tau_r \sim 10^{-8} - 10^{-9}$ sec lifetime of "free" excitons in solid Ne, the diffusion length of excitons

in this solid should exceed by one to two orders of magnitude the corresponding diffusion lengths previously determined for solid Ar and Xe. In the present paper we report the result of an experimental study of photoemission yields from pure solid Ne and from dilute impurity states of Ar, Kr and Xe in solid Ne in the energy range 8-30 eV. The major goal of the present study was to provide direct quantitative information regarding exciton dynamics in solid Ne as inferred from extrinsic photoemission data and from energy transfer to atomic impurity states. In that process we were able to obtain detailed information concerning two additional points. First, from the thresholds for direct photoemission from dilute atomic impurity states (point (e)) a firm value was established for the electron affinity of solid Ne confirming the results of recent EDC measurements^{11}. Second, new information was gathered regarding Auger type processes within a single atomic impurity centre.

On the basis of previous photoemission studies of the heavier rare gases we expect that in pure solid Ne two separate energy regimes for photoemission will be exhibited:

(AP) In the energy range $E_{n=1} \leq E \leq E_{TH}$ extrinsic photoemission takes place, which will exhibit a pronounced energy dependent structure in the excitonic region.

(BP) Above threshold, i.e. $E \geq E_{TH}$ intrinsic photoemission takes place.

For dilute impurity states in solid Ne three distinct energy regimes for photoemission are expected:

(AI) Direct photoemission from the impurity states above the impurity threshold, i.e. $E_{TH}^i \leq E \leq E_{n=1}$.

(BI) Exciton enhanced impurity photoemission resulting from energy transfer from the bound host exciton states to the impurity in the energy range $E_{n=1} \leq E \leq E_{TH}$.

(CI) Direct intrinsic photoemission from the host matrix at $E \geq E_{TH}$.

We have used the threshold for processes (AP) and (AI) to obtain information concerning V_0 for solid Ne. The energy dependence of the photoemission cross

sections in the range (AI) resulted in some information concerning Auger processes. Finally, and most interesting, we have utilized the host-impurity energy transfer data, mechanism (BI), to estimate the exciton diffusion length in solid Ne.

2. EXPERIMENTAL TECHNIQUES

The experiments were performed with the radiation of the DESY electron synchrotron. In the following we shall emphasize only those aspects of the apparatus and experimental procedures of particular importance for the present experiments. The experimental arrangement and the simultaneous optical and photoemission measurements have been described in detail elsewhere^{19,20}.

2.1 Apparatus, Determination of Photoemission Yields

Figure 2 shows the experimental setup for the simultaneous measurement of photoemission yield and reflectance spectra at liquid He temperature (~ 5 K) in the photon energy range 5 - 35 eV. Synchrotron radiation is monochromatized with a normal incidence grating instrument^{21}. The resolution is 2 Å over the whole spectral range, i.e. 0.1 eV at 25 eV. At the exit arm of the monochromator an ultrahigh vacuum chamber is attached. The system allows for measurements at pressures lower than 5×10^{-10} Torr.

The yield spectra were measured by a continuous scan of the incident photon energy. Photoelectrons were collected by a plane copper mesh of 75 % light transmittance in front of the emitting surface with an electric field of 2000 V/cm. Simultaneously the reflectance of the individual sample was recorded. It should be noted, that these reflectance spectra, which were further used for the determination of the yield per photon penetrating into the sample (see below), should not be regarded as being the reflectance from the particular rare gas film alone, because for these thin substrate-film sandwiches strong interference effects are still present (see e.g. Ref. 16).

For the determination of the absolute yield per incident photon the measured yield spectra were scaled to the photocurrent from the Au-substrate measured before condensation of the rare gas films. The absolute yield of Au was determined previously using a Samson double ionization chamber for absolute photon flux measurements^{20,22}. The measured yield curves were further corrected for the reflectance from the vacuum sample interface using the reflectance spectra measured simultaneously for the particular film studied as described in section 4.

For photon energies outside regions of strong absorption of the rare gas films (e.g. below the first exciton) one observes a contribution to the yield due to hot electrons excited at the Au substrate. A study of this contribution to the yield as a function of film thickness gives information about the scattering length L of electrons in the rare gas film (see section 3). The hot electrons have to be taken properly into account if one is interested in the intrinsic yield from the rare gas sample alone.

The film thickness of the samples was determined from the oscillations of the reflectance observed with increasing thickness during evaporation^{14,23}. For a nonabsorbing film, a condition fulfilled quite well for our samples for energies below the excitonic regions of the spectrum the change of the film thickness between two successive minima or maxima is given by $\Delta d = \lambda/2n$ where n is the refractive index of the film. Numerical data for the refractive index of Ne in the visible are available in the literature^{24}. The accuracy of the values for the thickness given with our results amounts to $\pm 10 \text{ \AA}$. The above procedure enabled us to study the thickness dependence of the photoemission, in particular the line shapes of the yield curves in detail.

2.2 Samples

The rare gases from L'Air Liquide and Matheson research, which were used as samples, had a purity of $\geq 99.995\%$ for Ne, 99.9997% for Ar, 99.995% for Kr, and $\geq 99.997\%$ for Xe. They have been used without further attempts for purification. The sample composition was controlled by mixing the appropriate amounts of the constituents in an ultrahigh vacuum gas handling system. The composition of the samples given with the results refers to the relative partial pressures of the total pressure of 1000 Torr in the gas handling

system. The thin films were prepared in situ by condensing the gases onto a cryogenically cooled gold substrate. Thus the concentrations cited present only a lower limit, because Ne and the impurity gases have much different sublimation temperatures and the true impurity concentration may have increased by a considerable factor^{14} upon solidification. Taking the known absorption coefficients of the impurity atoms^{2} we can estimate the enrichment factor from the absolute photoyield in the AI region and its dependence on the film thickness. It was in the range of 5 to 10. The optical spectra recorded simultaneously gave no indication for molecular impurities such as N₂, O₂ or H₂O.

3. INTRINSIC PHOTOEMISSION FROM PURE SOLID Ne

In Figure 3 we display the experimental photoemission yield, Y_m , from solid Ne deposited on a gold substrate at 6 K, for several values of the film thickness d in the range $d = 40-4300 \text{ \AA}$ in the energy region $E = 15 - 30 \text{ eV}$. The energy-dependent photoemission yield, $Y(E)$, from pure solid Ne was obtained from the data of Fig. 3, corrected for the reflectance R of the sample-substrate combination and for the direct photoemission from the gold substrate, so that

$$Y = \frac{Y_m}{(1 - R)} - Y_{Au}^0 \exp\{-d(k + \frac{1}{L})\} \quad (3.1)$$

where k is the absorption coefficient (Fig. 1), Y_{Au}^0 corresponds to the photoemission yield for pure gold and the escape length ($L \sim 3500 \text{ \AA}$) was assumed to be weakly energy dependent throughout the entire energy range. The later assumption is not bad as the corrections for the substrate photoemission are only important in the energy range 17-20 eV. The $Y(E)$ curves, Fig. 4, exhibit two distinct photoemission regimes. In the energy range above 21 eV a sharp rise of the photoemission yield is exhibited which corroborates earlier photoemission yield measurements for pure Ne⁶. The sharp rise is attributed to the onset of the intrinsic photoemission (range (BP)) in the pure solid. Unfortunately, a reliable determination of E_{TH} is difficult in view of the structure exhibited in the $Y(E)$ curves in the energy region 20-21.5 eV. We shall thus refrain from a quantitative determination of E_{TH} and subsequently of V_0 from the yield curve for the pure solid and utilize the photoemission data for impurity states

(section 5) for this purpose. In the intrinsic photoemission region, $E > 21$ eV, $Y(E)$ exhibits a marked thickness dependence at constant E , as is evident from Fig. 4. It arises from the low values of the absorption coefficients (Fig. 1), i.e. $k^{-1} \approx 300-1000 \text{ \AA}$ in that energy region, a fact which we have exploited for the determination of L in the next section.

4. ESCAPE LENGTH OF ELECTRONS IN SOLID Ne

The dependence of the yield Y on the thickness d for a fixed energy is different in the regions AP and BP. The thickness dependence of Y is displayed in Fig. 5 for a photon energy E representative for region BP. For $E = 25$ eV we have calculated the expected dependence of the yield Y with the escape length L as a parameter by use of

$$Y = \frac{1}{2} \frac{kL}{kL + 1} (1 - e^{-d(k + \frac{1}{L})}) \quad (4.1)$$

where we have used the experimentally determined k value (see Fig. 1). From Fig. 5 we conclude that $L \approx 3500 \text{ \AA}$ for Ne. This result is most sensitive to the absolute value of the yield which is accurate only within 20 %. Thus we can give a lower limit for L being 1500 \AA , whereas the upper limit can not be fixed accurately. The value of $L \approx 3500 \text{ \AA}$ for solid Ne is the largest one so far recorded for the escape length of hot electrons in a solid. It is comparable to the values of $L = 850 \text{ \AA}$ for solid Xe in the energy range $7.7-8.0 \text{ eV}^{\{18\}}$ and $L = 1200 \text{ \AA}$ for solid Ar in the energy region $8.0-9.2 \text{ eV}^{\{8\}}$. These L values for solid rare gases considerably exceed those observed for other materials. It is apparent that in the large-gap monoatomic insulators the mechanisms for energy loss are inefficient allowing for a long mean free path of hot electrons.

5. EXTRINSIC PHOTOEMISSION FROM SOLID NEON

Solid Ne exhibits extrinsic photoemission in the energy range $17-21$ eV (see Fig. 4) below the direct threshold, i.e. $E < E_{TH}$ for intrinsic photoemission. The quantum yield for this extrinsic photoemission is moderately low, below 9 %, the energy dependence of $Y(E)$ exhibits a pronounced structure, and $Y(E)$

at constant E is practically independent of the film thickness (see Fig. 6). The onset of the extrinsic photoemission coincides with the $n = 1$ exciton state and it spans the $n = 2$ exciton, as is evident from Figs. 1 and 4.

Similar extrinsic emission was previously observed from the heavier solid rare gases^{8}. Several mechanisms were considered for the physical origin of this extrinsic photoemission and will now be applied to the problem at hand. Exciton enhanced ionization of unidentified impurities in solid Ne can be rejected on the basis of the energy dependence of $Y(E)$ in the range 17-18 eV. Studies of exciton induced impurity ionization of Ar, Kr and Xe in solid Ne reported in sections 6 and 8 of the present paper reveal a photoemission line shape which exhibits a minimum at the maximum of the optical absorption line shape for the $n = 1$ state for film thicknesses exceeding $d \gtrsim 300 \text{ \AA}$. This effect should be practically independent of the nature of the impurity and is not observed in the extrinsic photoemission from the pure solid. Thus impurity effects are unlikely in the latter case. Non linear processes, such as exciton collisions or photoionization of exciton states can be ruled out for the weak light intensities employed herein, and, furthermore, Y is found to be independent of the comparatively low light intensity. A striking observation pertaining to the exciton diffusion process resulting in extrinsic photoemission from pure solid Ne is that the extrinsic yield is independent of the film thickness over the range $d = 40-4000 \text{ \AA}$, as is evident from Figs. 4 and 6. This behaviour drastically differs from that previously observed in pure solid Xe^{18} where Y versus d exhibits a maximum around $d \approx 200 \text{ \AA}$. Thus ionization of excitons at the insulator-vacuum interface is a serious possibility. In solid Ne the lowest $n = 1$ exciton state is located at 17.5 eV (while $E_{TH} \sim 21$ eV). A surface state which corresponds to the 1P_1 atomic excitation will be located even at a lower energy. We note, that evidence for surface states for solid Ne was obtained in earlier yield measurements^{6} and for all rare gas solids from recent absorption and reflection studies^{25}.

Next, one can argue that exciton states produced within the optical absorption depth, k^{-1} , are immobile and are operative in long range energy transfers to the gold substrate, resulting in electron photoejection from the gold. This mechanism, which is analogous the Förster-Dexter dipole-dipole coupling pro-

cess, should be characterized by a transfer distance d_o of the order of $d_o = 100 - 300 \text{ \AA}$. However, extrinsic photoemission from solid Ne at 17.5 eV, where $k^{-1} = 33 \text{ \AA}$ is exhibited for film thickness of $d = 4500 \text{ \AA}$, whereupon $d \gg d_o > k^{-1}$, ruling out this simple energy transfer process.

A further serious mechanism for the extrinsic photoemission in solid Ne originates from dynamic energy transfer by excitons. Exciton diffusion to the gold substrate is followed by electron ejection from the electrode. The energy transfer process at the metal-insulator interface will proceed by the Förster-Dexter mechanism involving the nonradiative decay of the exciton accompanied by the ionization of the metal. As effective extrinsic photoemission is exhibited (see Fig. 6) for thicknesses as large as $d \approx 4500 \text{ \AA}$ we have to assume that the diffusion length of excitons in pure solid Ne considerably exceeds the transfer length d_o ($\approx 100-300 \text{ \AA}$). The qualitative difference between the d dependence in solid Xe^{18} and in solid Ne may originate from the large "free" exciton diffusion length in the later case (see section 9).

6. PHOTOEMISSION FROM DILUTE ATOMIC IMPURITY STATES IN SOLID Ne

The photoemission yields from dilute alloys of Ar, Kr and Xe (impurity content 0.1-1.0 %) in solid Ne at 6 K were studied for film thicknesses $d = 50-4000 \text{ \AA}$ in the energy range 10-30 eV. Typical experimental data corrected just for the background emission from the gold substrate are displayed in Figs. 7-9. From simultaneous measurements of the optical reflectivity and photoemission the experimental yield curves were corrected for reflectance effects from the substrate-sample combination according to eq. (3.1). This procedure as applied to 1 % Kr alloy is outlined in Fig. 10.

In Fig. 11 we present the corrected photoelectric yield spectrum for 1 % Ar in Ne together with the reflectance from the doped sample. For the sake of comparison we have also presented in this figure the (corrected) yield spectrum from pure solid Ne. The energies of the impurity gap E_{TH}^i and of the band gap E_{TH} obtained from previous work are indicated by arrows. The photoemission spectrum of Ar/Ne (Fig. 11) as well as the yield spectra from Kr/Ne and Xe/Ne (see Figs. 8 and 9 for the uncorrected spectra) exhibit the three

intrinsic photoemission regimes expected for a doped solid, which are summarized in Table I. The onsets of the range (AI) provide reliable data for the impurity thresholds E_{TH}^i (section 7). The thickness dependence of $Y(E)$ in the region (AI) exhibits a gradual increase of Y at constant E , while the shape of the yield curve is quite independent of the film thickness. This d dependence of $Y(E)$ originates from incomplete absorption of the photons entering the sample and can be well accounted for in terms of eq. (4.1). In the range B(I) the exciton-enhanced impurity ionization yields exceed by one order of magnitude the extrinsic photoemission yield for pure solid Ne. In the thick ($d > 1000 \text{ \AA}$) doped solids at a doping level of 1 % the photoemission yield in this range reaches values close to 0.5, indicating complete exciton-impurity transfer. The line shapes for photoemission in the range (BI) and their thickness and concentration dependence will be discussed in section 8. Finally, in the range (CI) there is little difference between the pure solid and the dilute alloys.

7. ELECTRON AFFINITY OF SOLID NE FROM IMPURITY PHOTOEMISSION THRESHOLDS

The threshold energies for direct photoemission from atomic impurity states in solid Ne were determined utilizing a simple square root extrapolation near threshold. Fig. 12 provides an overview of the threshold regions, the resulting values of E_{TH}^i are summarized in Table II. Utilizing eq. (1.1) together with the spectroscopic values^{16} of E_G^i results in the V_O values summarized in Table II. These V_O values are independent of the nature of the impurity, thus providing strong additional support for the previous assignment of Wannier impurity states in solid Ne^{16}.

The high negative electron affinity, i.e. $V_O \equiv (-E_A) = + 1.2 \pm 0.2 \text{ eV}$ for solid Ne is in fair agreement with a previous theoretical estimate (V_O (theory) = + 0.54 eV)^{27}. In solid Ne, which consists of atoms characterized by a low polarizability, the contribution of the short range repulsive interactions, which is subsummed into a kinetic energy term, overwhelms the attractive term which originates from long-range polarization interactions, thus resulting in a large positive value of V_O . On the basis of these considerations it is apparent that also for liquid Ne V_O is large and positive,

although in the liquid we may expect that the relative importance of short-range repulsive interactions will be somewhat smaller than in the solid, whereupon V_0 (liq. Ne) < 1.2 eV. These considerations provide a proper rationalization for electron localization in liquid Ne, originating from short range repulsive interactions. Another piece of useful energetic data involves the polarization energy, P_+^i , of the medium by the positive impurity ion, which is given by $P_+^i = E_{Th}^i - I_g^i$, where I_g^i corresponds to the gas phase ionization potential. The values of P_+^i for Ar^{+g} , Kr^+ and Xe^+ in solid Ne are assembled in Table II. These polarization energies are substantially lower than those previously obtained for Kr^+ and Xe^+ in solid Ar and Xe^+ in solid Kr, reflecting the important role of long range polarization interactions in determining P_+^i . We note in passing that short range repulsive interactions are of some importance in this context as is evident from the fact that P_+^i for Ar^+/Ne is lower than the corresponding value of P_+^i for the Kr^+/Ne and Xe^+/Ne systems, while P_+^i for the latter two systems are practically identical.

8. AUTOIONIZATION AND INTRACENTRE AUGER PROCESSES IN DILUTE Ne ALLOYS

We shall now dwell briefly on the nature of metastable exciton and impurity states in solid Ne. As it is well known, excited states located above $E_G(3/2)$ (or $E_G^i(3/2)$) in solid rare gases are metastable with respect to internal autoionization to the conduction band. In pure solid Ne with $E_{TH} = E_G - V_0 = 20.5$ eV and $E_G = 21.69$ eV, the vacuum level is located 1.2 eV below the interband threshold. Thus the $n = 3$ and higher exciton states (see Fig. 1) in the pure solid are metastable with respect to autoionization into the vacuum. In a similar manner on the basis of the energetic data presented in Table II together with the spectroscopic data for the dilute Ne alloys^{16} we can assert that the $n = 3$ (3/2) states in Ar/Ne , Kr/Ne and Xe/Ne , where we have listed only those (3/2) impurity Wannier states which were observed in absorption, are all metastable with respect to autoionization into the vacuum. On the other hand the $n = 3$ (3/2) states are stable with respect to internal autoionization into the conduction band.

From the foregoing considerations we expect a pronounced contribution to the photoemission yield in the energy range (AI) originating from excitation to $n = 3$ ($3/2$) states and also to the $n = 3$ ($1/2$) state which involves the same final one-electron level in Ar/Ne, Kr/Ne and Xe/Ne. As for these dilute impurity states in Ne $kL \approx 0.1$ for the $n = 3$ ($3/2$, $1/2$) level (at 1 % impurity content) then from eq. (4.1) we assert that the photoemission yield curves in the range (AI) should exhibit pronounced peaks around the $n = 3$ ($3/2$) and the $n = 3$ ($1/2$) states in these alloys. The real life situation is more complex and more interesting, as is evident from Fig. 13 where we display the $Y(E)$ curves in the range (AI) together with a schematic representation of the positions of the Wannier states. Several experimental observations are worth recording. First, the $n = 1$ and $n = 2$ ($3/2$) and the $n = 1$ ($1/2$) states do not contribute to the photoemission yield, as these states are located below E_{TH}^i in all cases. Second, the $n = 3$ ($1/2$) states contribute to the photoemission yield, as expected. Third, the $n = 2$ ($1/2$) state in Xe/Ne, Kr/Ne and possibly also in Ar/Ne (where in the latter case $n = 2$ ($1/2$) and $n = 3$ ($3/2$) states are close) contribute to the photoemission yield. In Table III we compare the positions of the $n = 2$ ($1/2$) peaks in the photoemission curves with the corresponding Wannier levels obtained from optical data^{16}. This last result is of interest as it provides new information regarding non radiative Auger type processes within a single impurity centre in solid Ne.

The $n = 2$ ($1/2$) state for these atomic impurities cannot decay directly above the vacuum level as the (one electron) energy of the $n = 2$ excited Wannier orbital is lower than E_{TH}^i . The $n = 2$ ($1/2$) state can decay nonradiatively via two channels: (a) Electronic relaxation $n = 2$ ($1/2$) \rightarrow $n = 1$ ($1/2$) to the lower Wannier state, which is stable with respect to autoionization into the vacuum. (b) Auger type ionization resulting in a guest atom in the ($3/2$) state and an electron above the vacuum level. This Auger type intracentre autoionization process is schematically described in Fig. 14.

From the experimental data we conclude that channel (b) is at least as fast as channel (a), i.e. $\tau(n = 2 \rightarrow n = 1) \gtrsim \tau(\text{Auger})$. Theoretical calculations by Webman and Jortner^{28} of nonradiative multiphonon relaxation processes between impurity states in solid rare gases result in $\tau(n = 2 \rightarrow n = 1) \approx 5 \times 10^{-13}$ sec for the $n = 2 \rightarrow n = 1$ relaxation in solid Ne. Thus $\tau(\text{Auger}) \leq 10^{-13}$ sec.

9. EXCITON INDUCED IMPURITY IONIZATION IN SOLID NEON

Photoemission from lightly doped Ne in the region (BI) was assigned to electronic energy transfer to impurity states resulting in exciton induced impurity photoionization (see Fig. 15). The photoyield curves for 1 % atomic impurity concentration at several film thicknesses, corrected for substrate photoemission and for reflection effects, are displayed in Fig. 16-18. The qualitative features of these photoemission yield curves are similar to those previously observed and discussed for the Xe/Ar system^{8}. In particular, we notice that at high values of d ($> 200 \text{ \AA}$) the yield exhibits a minimum at 17.5 eV which corresponds to the maximum of the $n = 1$ state, while for thinner films ($d < 200 \text{ \AA}$) the minimum at 17.5 eV is replaced by a maximum. At higher energies $Y(E)$ exhibits maxima at 20.3 eV, at 21.1 eV and at 21.4 eV which practically coincide with the $n = 2$, $n = 3$ and $n = 4$ excitonic levels of pure Ne. The energy dependence and the d dependence of the yield in the energy range 17-18 eV cannot be reconciled with a simple model involving electronic energy transfer from immobile excitons to the impurity state. Such a model will result in $Y(E)$ at constant impurity concentration being proportional to eq. (4.1) and thus cannot explain the dips in the $Y(E)$ curves at 17.5 eV for large d . The experimental data were interpreted in terms of the exciton diffusion model previously advanced by us^{8} which rests on the following assumptions:

- (1) The escape length L is a weakly varying function of the energy over the energy range 17-23 eV, being given by $l = 3500 \text{ \AA}$ (see section 3).
- (2) The exciton diffusion length at a given impurity concentration is constant for all excitation energies. This assumption implies that the rate of the radiationless relaxation of higher ($n > 1$) exciton states to the lowest $n = 1$ state is large on the time scale of the exciton lifetime. In light of Webman's calculations^{28} which result in $\tau(n = 2 \rightarrow n = 1) \approx 5 \times 10^{-13}$ sec in solid Ne this assumption is reasonable. Direct experimental support for this assumption originates from electron energy distribution measurements from mixtures of 1% Xe in Ne. In these recent experiments^{29} it was shown, that the kinetic energy of electrons produced in range (BI) is independent of the excitation energy in the range 17.5 - 20.5 eV spanning the $n = 1$ and $n = 2$ exciton states. Thus even at 1 % Xe concentration the $n = 2 \rightarrow n = 1$ relaxation pro-

cess between exciton states precedes the exciton impurity energy transfer process.

The exciton diffusion model involving competition between energy transfer and decay of excitons results in the following expression for the photo-emission yield:

$$Y(E) = S\tau([R]) \ell^{(R)} F\{\ell^{(R)}, L, k(E), d\} \quad (9.1)$$

$$F\{\ell^{(R)}, L, k(E), d\} = \frac{k}{k^2 \ell^2 - 1} \left\{ \frac{A \cdot L \cdot \ell}{L + \ell} \left[1 - \exp\left(-\frac{d}{\ell} - \frac{d}{L}\right) \right] + \frac{B \cdot L \cdot \ell}{\ell - L} \left[1 - \exp\left(\frac{d}{\ell} - \frac{d}{L}\right) \right] - \frac{L}{kL + 1} \left[1 - \exp\left(-kd - \frac{d}{L}\right) \right] \right\} \quad (9.2)$$

$$A = \frac{\exp(-kd) - \exp(d/\ell)}{\exp(-d/\ell) - \exp(d/\ell)} \quad (9.3)$$

$$B = \frac{\exp(-d/\ell) - \exp(-kd)}{\exp(-d/\ell) - \exp(d/\ell)} \quad (9.4)$$

$$\ell^{(R)} = \ell_0 (1 + S\tau_0 [R])^{-1/2} \quad (9.5)$$

$$\ell_0 = (D\tau_0)^{1/2} \quad (9.6)$$

$$\tau([R]) = \left(\frac{1}{\tau_0} + S [R] \right)^{-1} \quad (9.7)$$

where S is the rate constant for impurity ionization, $[R]$ is the impurity concentration, $\tau_0 \approx 10^{-8} - 10^{-9}$ corresponds to the exciton lifetime in the pure crystal, $\tau([R])$ represents the lifetime of the exciton in the doped crystal, ℓ_0 denotes the exciton diffusion length in the pure crystal, with D being the exciton diffusion coefficient, while $\ell^{(R)}$ is the exciton diffusion length in the doped crystal. The procedure for fitting of the absolute quantum yields for different values of d and $[R]$ to the two parameters ℓ_0 and $S\tau_0$ is similar to that previously employed^{8} and will not be repeated in detail. In Figs. 19 and 20 we display the results of model calculations of $Y(E)$ according to eqs. (9.1) - (9.7) taking $S\tau_0 [R] = 1$ for various values of ℓ using the $k(E)$ values from Fig. 1 and $L = 3500 \text{ \AA}$. In particular we note that the

dip at 17.5 eV for large d is enhanced with increasing ℓ . For small values of d a maximum appears at this energy while the excitonic structure of the higher members of the Wannier series follows the peaks in the absorption spectrum. An excellent fit of the experimental data for 1 % impurity concentration in Ar/Ne, Kr/Ne and Xe/Ne was accomplished over a broad range of d values (Figs. 16-18) using $\ell(R) = 20-30 \text{ \AA}$ at 1 % impurity concentration for all systems. The concentration dependence of $Y(E)$ for Ar/Ne at $d = 450 \text{ \AA}$ is presented in Fig. 21 where the best agreement with experiment is accomplished taking $\ell(R) = 70 \text{ \AA}$ to 90 \AA at 0.1 % impurity concentration. Finally the parameter $S\tau_0$ was estimated from data in the energy region corresponding to the $n = 2$ exciton states. From Fig. 22 we conclude that the best fit between theory and experiment is accomplished taking $S\tau_0 \geq 10^{-2} (\text{ppm})^{-1}$ or $S\tau_0 \geq 6 \times 10^{-19} \text{ cm}^3$. The absolute quantum yield for different Ar concentrations is according to Fig. 22 nearly independent of $S\tau_0$ for values of $S\tau_0$ larger than $10^{-2} (\text{ppm})^{-1}$. Therefore the experimental data give only this lower limit for $S\tau_0$ {30}.

Taking the probable value $S\tau_0 = 10^{-17} \text{ cm}^3$ together with $\ell_1, |R_1|$ or $\ell_2, |R_2|$ we obtain with the aid of eq. (9.5) the value $\ell_0 = 2500 \pm 500 \text{ \AA}$ for the diffusion length of excitons in pure solid Ne. The diffusion coefficient of excitons in solid Ne is now estimated from eq. (9.6) with $\tau_0 = 10^{-9}$ sec resulting in $D \approx 0.9 \text{ cm}^2/\text{sec}$. Finally, we estimate $S \approx 10^{-8} \text{ cm}^3 \text{ sec}^{-1}$ for the rate constant for exciton enhanced impurity ionization in solid Ne.

10. CONCLUDING REMARKS

In this paper we have demonstrated how photoemission data can be utilized to extract new information concerning energetics, nonradiative relaxation phenomena and exciton dynamics in solid Ne. Concerning energetic data we were able to establish experimentally a definite value for V_0 in this solid, which concurs with recent EDC photoemission data {11}. Regarding non radiative relaxation phenomena we have established that the $n = 2 (1/2) \rightarrow M^+ (3/2) + e$ (vacuum) process occurs on the time scale $\tau(\text{Auger}) \leq 10^{-13}$ sec which is comparable or even shorter than the $\tau(n = 2 \rightarrow n = 1)$ non radiative relaxation process. On the other hand the EDC photoemission data {29} for 1 % Xe/Ne in

the energy range 17.5 - 20.5 eV demonstrate that $\tau(n = 2 \rightarrow n = 1) \ll \tau$, where τ is the exciton lifetime in the doped solid, which according to eq. (9.7) and $S\tau_0 = 10^{-17} \text{ cm}^{-3}$ is $\tau \approx 10^{-11}$ sec at 1 % impurity, a conclusion compatible with the theoretical estimate^{28} $(n = 2 \rightarrow n = 1) \approx 5 \times 10^{-13}$ sec. We were thus able to establish a hierarchy for time scales of nonradiative relaxation phenomena in this system. Finally detailed information concerning exciton dynamics in solid Ne was obtained, which is summarized in Table IV together with relevant data for other solid rare gases.

From these results the following unified picture emerges:

- (a) The exciton diffusion length in all solid rare gases considerably exceeds the lattice spacing
- (b) The approximate value of l_0 in solid Ne exceeds the corresponding values in Xe and Ar by about one order of magnitude. This result is compatible with the lifetime ratio of "free" excitons. As exciton trapping in solid Ne below 6K does not occur

$$\left[\tau_0(\text{Ne})/\tau_0(\text{Ar, Xe}) \right]^{1/2} \approx 30 \quad (10.1)$$

- (c) The free exciton diffusion coefficient is similar in all solid rare gases.
- (d) The products $S\tau_0$ in solid Ne exceeds that in solid Ar and Xe by three orders of magnitude, a result compatible with the lifetime ratio (10.1).
- (e) The rate constants for exciton photoionization S are similar in all solid rare gases.
- (f) The rate constants $S \approx \pi R_a^2 D/\Lambda$ where $R_a \approx 10 \text{ \AA}$ is the reaction radius can be utilized to extract the estimate $\Lambda \sim 3 \text{ \AA}$ for the mean free path for exciton scattering in all solid rare gases. Thus $\Lambda \sim a$ and the exciton motion is diffusive in all these simple solids at low temperatures.

Table I Photoemission ranges in doped solid Ne (energies in eV)

	AI	BI	CI
	$E_{TH}^i \leq E \leq E_{n=1}$	$E_{n=1} \leq E \leq E_{TH}$	$E \geq E_{TH}$
Ar in Ne	15.05 - 17.48	17.48 - 20.5	20.5 - 30.0
Kr in Ne	13.48 - 17.48	17.48 - 20.5	20.5 - 30.0
Xe in Ne	11.60 - 17.48	17.48 - 20.5	20.5 - 30.0

Table II Values for the energy gap E_G , E_G^i , the gas phase ionization potential I_g , the threshold energy E_{TH} , E_{TH}^i , $V_o (\equiv -E_A)$ and the polarization energy P_+ , P_+^i .

	E_G or E_G^i	$I_g^{(a)}$	E_{TH} or E_{TH}^i	$V_o (\equiv -E_A)$	P_+ or P_+^i
Ne (pure)	21.69	21.56	20.3 ^(b)	1.4 ^(b)	-1.3 ^(b)
Ar in Ne	16.23	15.68	15.05	1.18	-0.63
Kr in Ne	14.78	13.92	13.48	1.30	-0.45
Xe in Ne	12.63	12.08	11.60	1.03	-0.48

(a) The values for the gas phase ionization potential have been taken from: C. Moore, NBS Circular 467 Vol. III (1952)

(b) Results from energy distribution measurements: N. Schwentner, F.-J. Himpsel, V. Saile, M. Skibowski, W. Steinmann, and E.E. Koch, Phys.Rev.Lett. 34, 528 (1975)

Table III Exciton energies $E_{n=2}^i$ (1/2) impurity excitons from the yield spectra (Fig. 13). Values in brackets are taken from optical reflection peaks.
 E_{TH}^i is the threshold energy of the impurity, ζ the spin-orbit splitting of the guest atoms.

	$E_{n=2}^i$ (1/2)		$E_{n=2}^i(1/2) - E_{TH}^i$	ζ
Ar in Ne	15.35	(15.31)	0.30	0.34
Kr in Ne	14.09	(14.06)	0.61	0.61
Xe in Ne	12.62	(12.59)	1.03	1.27

Table IV Parameters describing the diffusion of "free" excitons in the rare gas solids.

	Xe (a,b)	Ar (c)	Ne (d)
L (Å)	850	1200	3500
t_o (sec)	$10^{-12} - 10^{-11}$	$10^{-12} - 10^{-11}$	$10^{-9} - 10^{-8}$
λ_o (Å)	170 ^(e) 300 ^(f)	120 ^(e)	2500 ^(e) (200 (g))
St_o (cm ³)	$6 \cdot 10^{-19}$	$6 \cdot 10^{-20}$	10^{-17}
S (cm ³ sec ⁻¹)	C ₆ H ₆ in Xe 10^{-7}	Xe in Ar 10^{-8}	Xe, Kr, Ar in Ne 10^{-8}
D (cm ⁻² sec ⁻¹)	0.3 - 0.9	1	0.9

(a) Z. Ophir, B. Raz, and J. Jortner, Phys. Rev. Lett. 33, 415 (1974)

(b) Z. Ophir, B. Raz, N. Schwentner, M. Skibowski, and J. Jortner, J. Chem. Phys., in press

(c) Z. Ophir, B. Raz, J. Jortner, V. Saile, N. Schwentner, E.E. Koch, M. Skibowski, and W. Steinmann, J. Chem. Phys. 62, 650 (1975)

(d) present work

(e) Exciton enhanced impurity photoionization

(f) Extrinsic photoemission

(g) Lower limit see footnote {30}.

References

1. Rare Gas Solids, edited by M.K. Klein and J.A. Venables, Academic Press, New York, in press
2. For a recent review see: B. Sonntag, Optical Properties in Ref. 1
3. J.F. O'Brien and K.J. Teegarden, Phys.Rev.Lett. 17, 919 (1966)
4. N. Schwentner, M. Skibowski, and W. Steinmann, Phys.Rev. B8, 2965 (1973)
5. E.E. Koch, B. Raz, V. Saile, N. Schwentner, M. Skibowski, and W. Steinmann, Jap.J.Appl.Phys.Suppl. 2, Pt2, 1974 ,p. 775
6. E.E. Koch, V. Saile, N. Schwentner, and M. Skibowski, Chem.Phys.Letters 28, 562 (1974)
7. Z. Ophir, B. Raz, and J. Jortner, Phys.Rev.Lett. 33, 415 (1974)
8. Z. Ophir, B. Raz, J. Jortner, V. Saile, N. Schwentner, E.E. Koch, M. Skibowski, and W. Steinmann, J.Chem.Phys. 62, 650 (1975)
9. I.T. Steinberger, E. Pantos, and I.H. Munro , Phys.Letters 47A, 299 (1974)
10. N. Schwentner, F.-J. Himpsel, E.E. Koch, V. Saile, and M. Skibowski, in Vacuum Ultraviolet Radiation Physics, edited by E.E. Koch, R. Haensel and C. Kunz, Pergamon-Vieweg, 1974 ,p. 335
11. N. Schwentner, F.-J. Himpsel, V. Saile, M. Skibowski, W. Steinmann, and E.E. Koch, Phys.Rev.Lett. 34, 528 (1975)
12. A.B. Kunz, D.J. Mickish, S.K.V. Mirmira, T. Shima, F.-J. Himpsel, V. Saile, N. Schwentner, and E.E. Koch, submitted to Solid State Communications
13. For a recent review see: J. Jortner, Electronic Excitations in molecular Crystals, in Vacuum Ultraviolet Radiation Physics, edited by E.E. Koch, R. Haensel, and C. Kunz, Pergamon-Vieweg, Braunschweig 1974, p. 263
14. G. Baldini, Phys.Rev. 137A, 508 (1965)
15. A. Gedanken, B. Raz, and J. Jortner, J.Chem.Phys. 58, 1178 (1973)
16. D. Pudewill, F.-J. Himpsel, V. Saile, N. Schwentner, M. Skibowski, and E.E. Koch, submitted to phys.stat.sol. (b)

17. A. Gedanken, B. Raz, and J. Jortner, J. Chem.Phys. 59, 5471 (1973)
18. Z. Ophir, N. Schwentner, B. Raz, M. Skibowski, and J. Jortner, J.Chem.Phys., in press
19. N. Schwentner, A. Harmsen, E.E. Koch, V. Saile, and M. Skibowski, in: Vacuum Ultraviolet Radiation Physics, ed. by E.E. Koch, R. Haensel, and C. Kunz, Pergamon-Vieweg, Braunschweig, 1974, p.792
20. N. Schwentner, thesis Universität München, München (1974) and DESY F41-75/04 (1975), internal report
21. M. Skibowski and W. Steinmann, J. Opt. Soc. Am. 57, 112 (1967) and E.E. Koch and M. Skibowski, Chem.Phys.Lett. 9,429 (1971)
22. U. Backhaus, Diplomarbeit, Universität Hamburg (1973)
23. A. Harmsen, Diplomarbeit, Universität Hamburg (1975)
24. J. Kruger and W.J. Ambs, J.Opt.Soc.Am. 49, 1195 (1959)
25. V. Saile et al., to be published
26. In view of the large diffusion length $\ell_0 \sim 3000 \text{ \AA}$ we can safely assume that $\ell_0 \gg d_0$, where d_0 is the transfer length from excitons to the gold substrate. Thus for solid Ne corrections to eq. 5.1, which assumes energy transfer at $x = d$, will be small.
27. B.Raz and J. Jortner, Chem.Phys.Lett. 4, 155 (1969)
28. I. Webman and J. Jortner, to be published
29. N. Schwentner and E.E. Koch, to be published

30. A lower limit for ℓ_0 may be established as follows:

Using the two sets of diffusion length and concentration $\ell_1 = 25 \pm 5 \text{ \AA}$, $[R_1] = 10^4 \text{ ppm}$ and $\ell_2 = 70 \text{ \AA} \pm 20 \text{ \AA}$, $[R_2] = 10^3 \text{ ppm}$ the diffusion length ℓ_0 of pure Ne can be determined eliminating $\sigma\tau_0$ from eq. (9.5):

$$\ell_0 = \ell_1 \cdot \ell_2 \left(\frac{[R_1] - [R_2]}{\ell_1^2 [R_1] - \ell_2^2 [R_2]} \right)^{1/2}$$

with $\ell_1 = 25 \text{ \AA}$ and $\ell_2 = 70 \text{ \AA}$ we get $\ell_0 = 150 \text{ \AA}$. This value has to be considered with care because of the results of this eq. are very

sensitive to λ_1 and λ_2 . For example for $\lambda_1 = 25 \text{ \AA}$ and $\lambda_2 = 79 \text{ \AA}$, values within the experimental error, $\lambda_0 \rightarrow \infty$. But with eq. (9.5) and the above stated lower limit for $\text{St}_0 = 10^{-2} (\text{ppm})^{-1}$ we get with $\lambda_1, [R_1]$ as well as with $\lambda_2, [R_2]$ the same lower limit for λ_0 : $\lambda_0 > 200 \text{ \AA}$.

Figure Captions

- Fig. 1 Absorption coefficient k of pure solid Ne for photon energies from 15 to 25 eV.
- Fig. 2 Experimental arrangement for the simultaneous measurement of photoemission yield and reflectance spectra at liquid He temperatures in the photon energy range 5-35 eV. ES exit slit of the monochromator, MP photomultiplier, SH cryo-shields, S sample holder, Q quartz substrate, Au gold film, C copper mesh, NV needle valve.
- Fig. 3 Photoelectric yield spectra of pure Ne in the range $h\nu = 15-30$ eV for different film thicknesses. The spectra are not corrected for the electron contribution from the gold substrate and the reflectance. The photoelectric yield curve of the gold substrate is also shown.
- Fig. 4 Photoelectric yield of pure Ne on Au for six different film thicknesses. The spectra are corrected for the hot electron contribution from the gold substrate and the reflectance.
- Fig. 5 Dependence of the photoyield for pure Ne on the film thickness at $h\nu = 25.0$ eV (above threshold). The solid curves give the calculated yield according to eq. 4.1 varying the electron escape length L and taking $k = 0.0019 \text{ \AA}^{-1}$ (see Fig. 1).
- Fig. 6 Dependence of the photoyield for pure Ne on the film thickness at $h\nu = 17.5$ eV (excitonic part of the spectrum).
- Fig. 7 Photoelectric yield for 1 % Ar in Ne for four different film thicknesses. The spectra have not been corrected for the reflectance. A constant contribution to the total yield from the Au substrate has been subtracted.
- Fig. 8 Photoelectric yield for 1 % Kr in Ne for four different film thicknesses. The spectra have not been corrected for the reflectance. A constant contribution to the total yield from the Au substrate has been subtracted.
- Fig. 9 Photoelectric yield for 1 % Xe in Ne for four different film thicknesses. The spectra have not been corrected for the reflectance. A constant contribution to the total yield from the Au substrate has been subtracted.

- Fig. 10 Photoyield (solid curve), reflectance (dash-dotted curve) and corrected photoyield (dashed curve) for thin Ne films, doped with 1 % Kr on Au substrates in the range of the first Ne exciton. For details see text.
- Fig. 11 Photoelectric yield per photon penetrating into the sample for 1 % Ar in Ne (solid curve) and pure Ne (dashed curve). The insert shows the reflectance measured simultaneously.
- Fig. 12 Onset of impurity photoelectron emission for Xe in Ne, Kr in Ne and Ar in Ne. Data have been obtained for the film thickness given for each curve. Note that the $(\text{yield})^{1/2}$ spectra are in arbitrary units, which, however, are the same for the three curves.
- Fig. 13 Photoelectric yield for 1 % Xe in Ne, 1 % Kr in Ne and 1 % Ar in Ne in the range of onset of direct photoemission from the Xe, Kr and Ar impurity levels. The positions of the exciton bands from the impurities as well as the limit they converge to are indicated.
- Fig. 14 Energy levels involved in the Auger-type recombination process of the $n \geq 2$ ($\Gamma 1/2$) impurity excitons.
- Fig. 15 Schematic scheme of the energy levels involved in photoelectron emission from solid neon doped with Ar, Kr and Xe. VB valence band, CB conduction band, E_{TH} vacuum level, $E_A \equiv -V_o$ electron affinity, E_G gap energy, E_G^i gap energy for the impurities, exciton states of the host matrix and of the impurities are indicated.
- Fig. 16 Comparison of measured (solid curves) and calculated photoemission yield spectra (dashed curves) for 1 % Ar in Ne for various film thicknesses. The calculation was carried out with $L = 3500 \text{ \AA}$ for the electron escape length, $l = 20 \text{ \AA}$ for the diffusion length, and $S \cdot \tau [\bar{R}] = 1$.
- Fig. 17 Comparison of measured (solid curves) and calculated photoemission yield spectra (dashed curves) for 1 % Kr in Ne for various film thicknesses. The calculation was carried out with $L = 3500 \text{ \AA}$ for the electron escape length, $l = 20 \text{ \AA}$ for the diffusion length, and $S \cdot \tau [\bar{R}] = 1$.

- Fig. 18 Comparison of measured (solid curves) and calculated photoemission yield spectra (dashed curves) for 1 % Xe in Ne for various film thicknesses. The calculation was carried out with $L = 3500 \text{ \AA}$ for the electron escape length, $l = 20 \text{ \AA}$ for the diffusion length and $S \cdot \tau [R] = 1$.
- Fig. 19 Calculated photoemission yield spectra for three different film thicknesses for doped Ne films. The electron escape length is taken to be $L = 3500 \text{ \AA}$, the exciton diffusion length l is varied in steps of 10 \AA .
- Fig. 20 Calculated dependence of the photoemission yield spectra for doped Ne films on the film thickness d . The electron escape length L is taken to be 3500 \AA , the exciton diffusion length l is taken to be 20 \AA , and $S \cdot \tau [R] = 1$.
- Fig. 21 Comparison of measured (thick solid curves) and calculated photoemission yield spectra (thin curves) for 1 % and 0.1 % Ar in Ne. For both measurements the film thickness was $d = 450 \text{ \AA}$. The calculation was carried out with $L = 3500 \text{ \AA}$ for the electron escape length, $S \cdot \tau [R] = 1$ and $l = 20, 30 \text{ \AA}$ and $l = 60, 90, 100 \text{ \AA}$ for 1 % and 0.1 % Ar concentration respectively.
- Fig. 22 Calculated concentration dependence of the photoemission yield for 1% Ar in Ne for the $n = 2$ exciton using a film thickness of 450 \AA . The yield was calculated for different parameters $S\tau_0$. The two experimental points (dots) favour the lower values for $S\tau_0$ ($1-10^{-2}$).

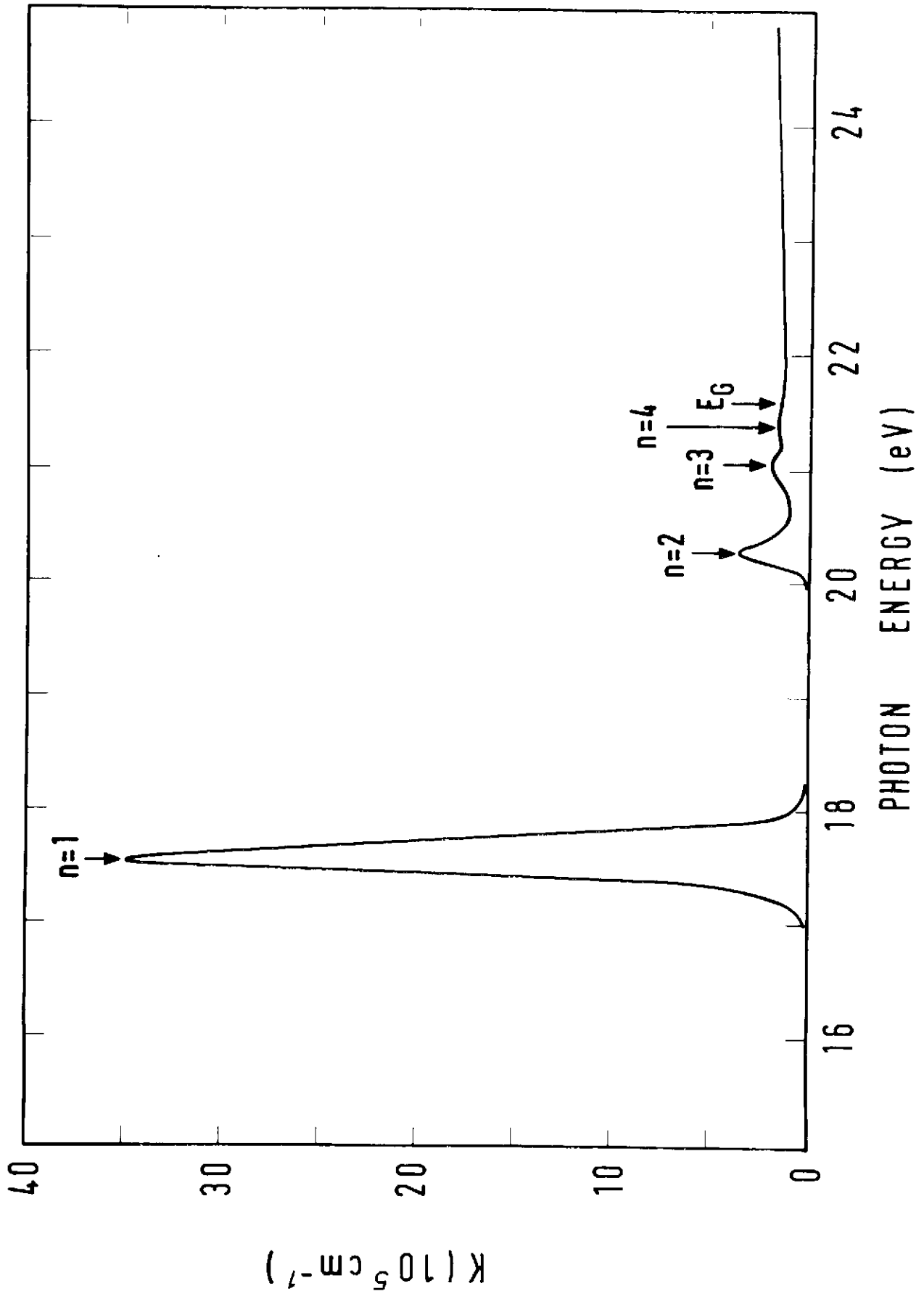


FIG. 1

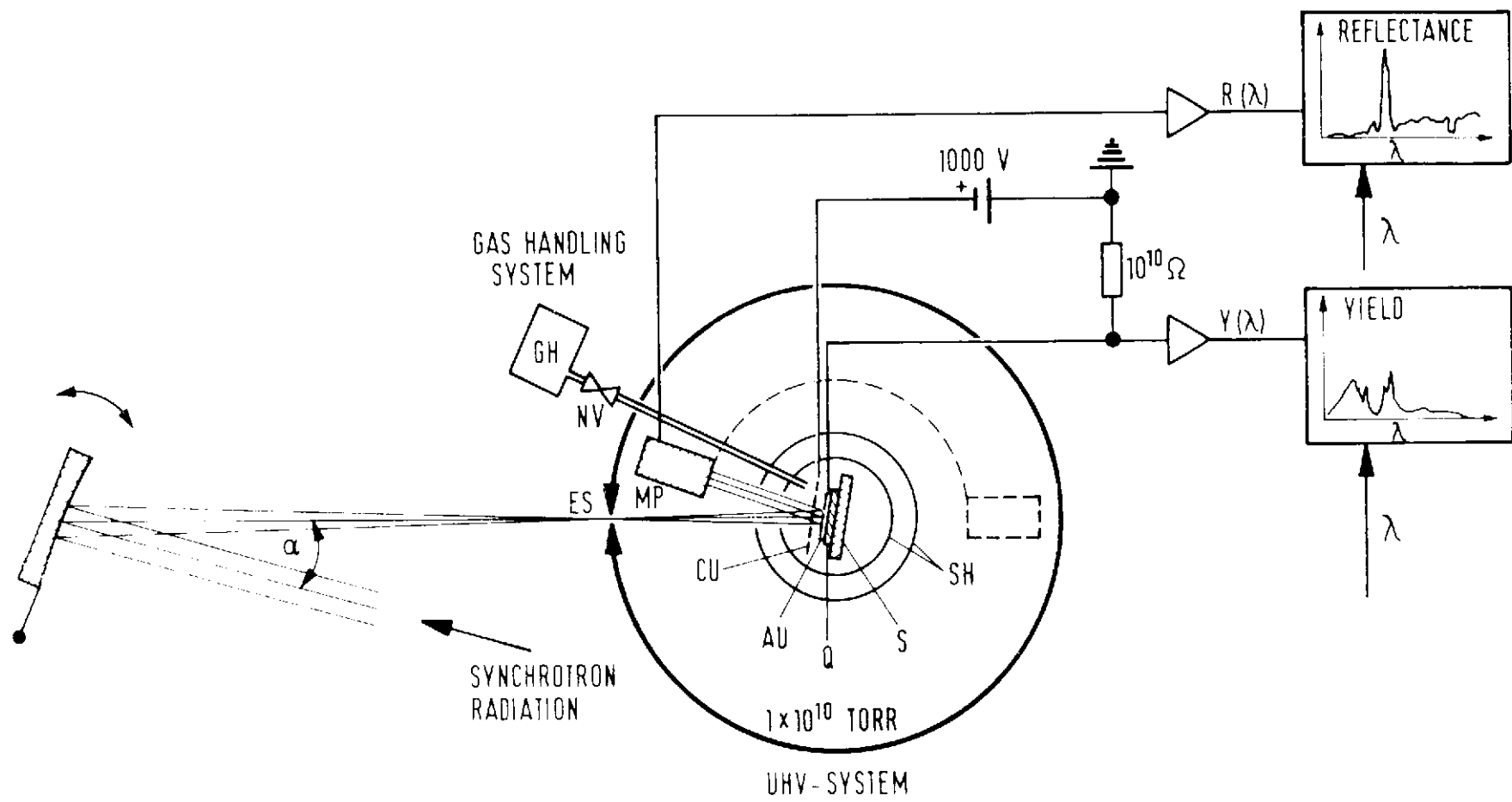


Fig. 2

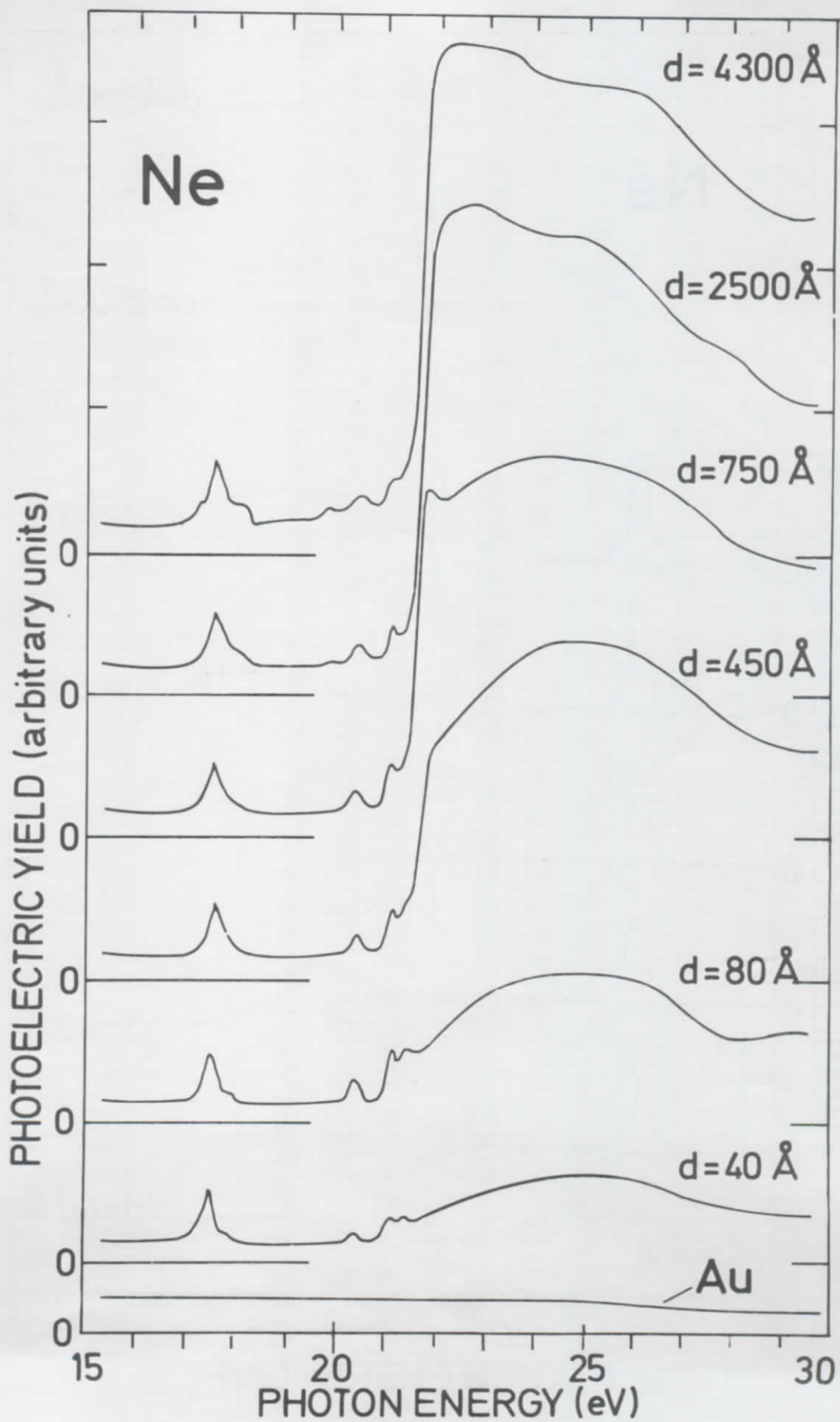


Fig. 3

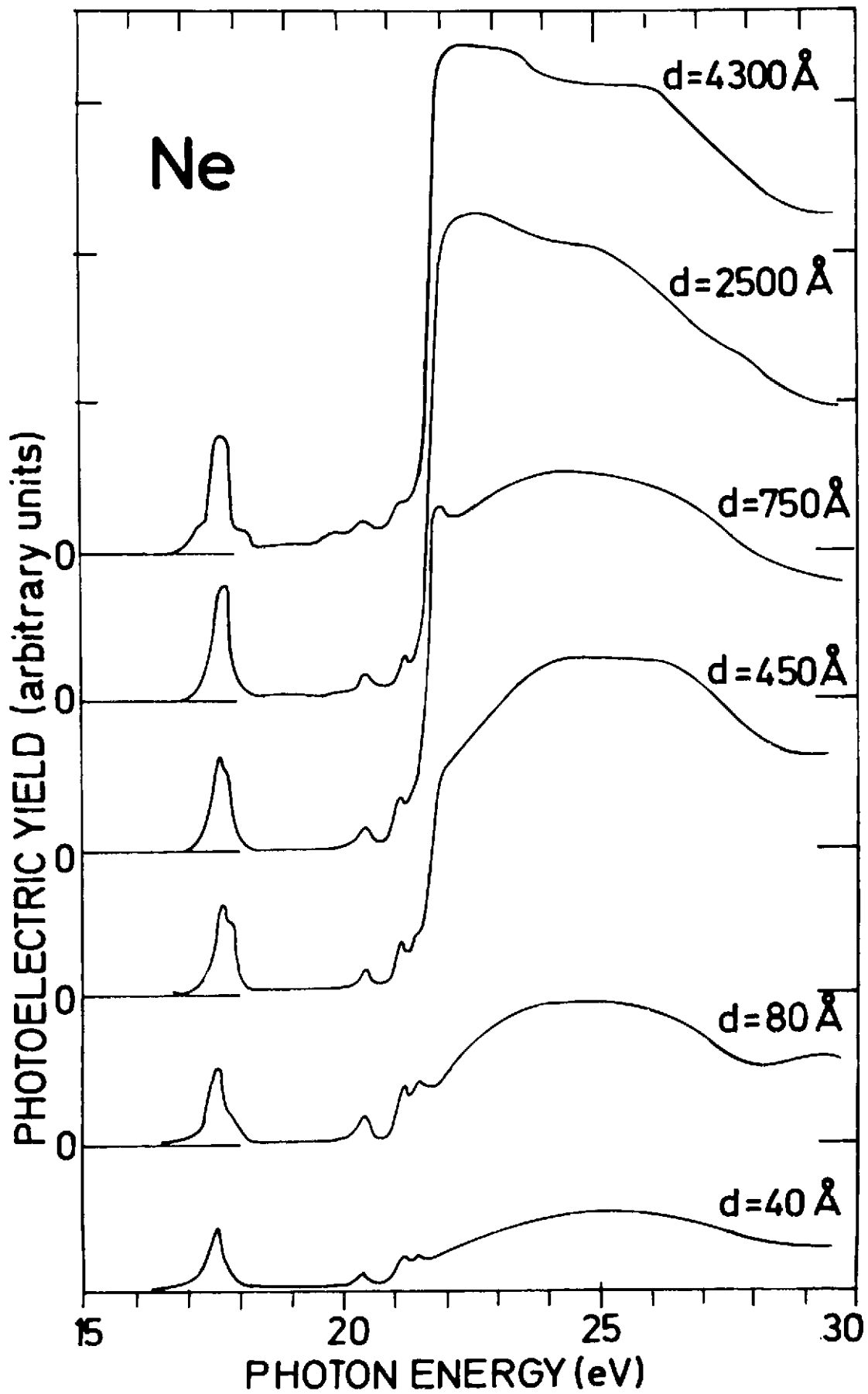


FIG. 4

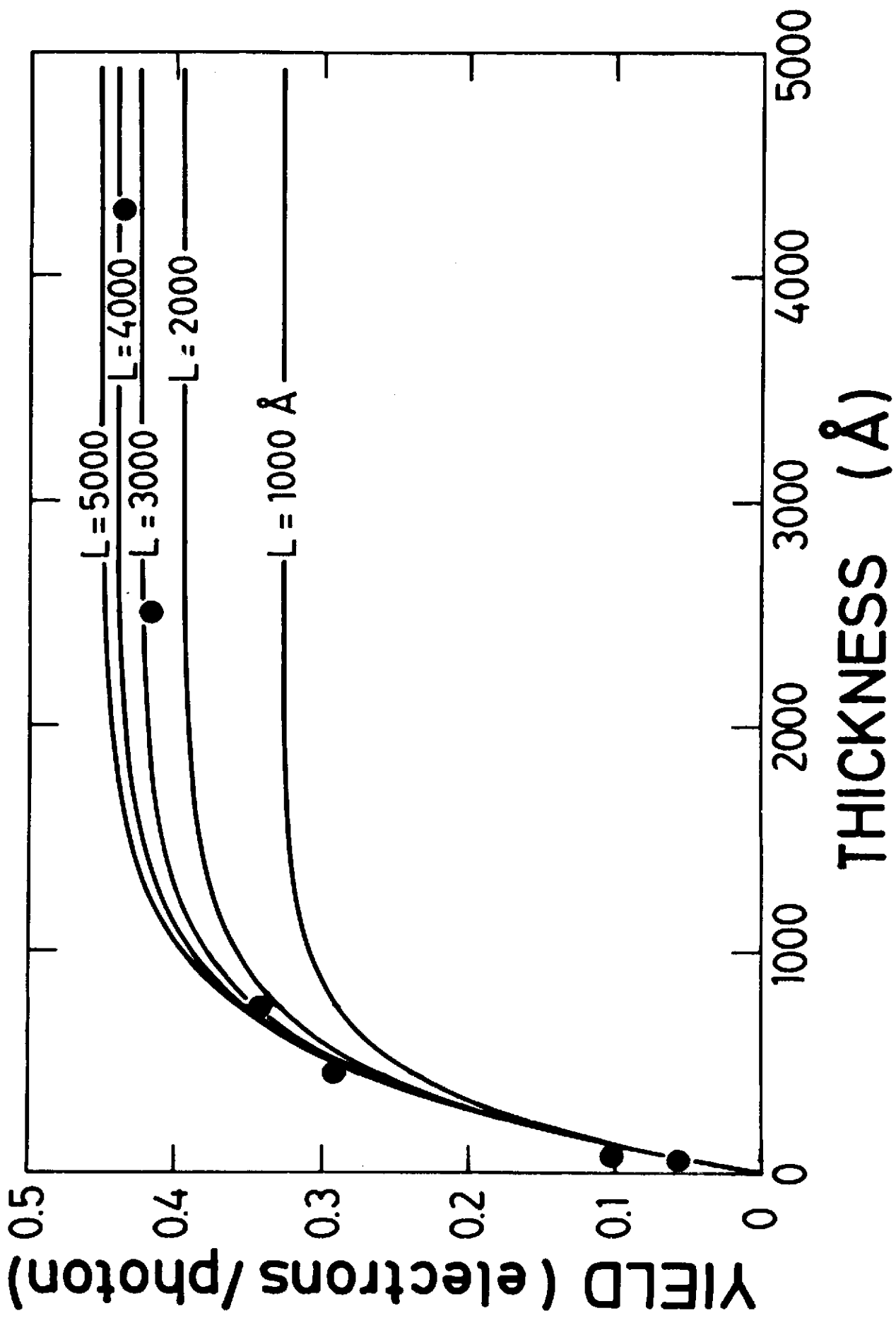


FIG. 5

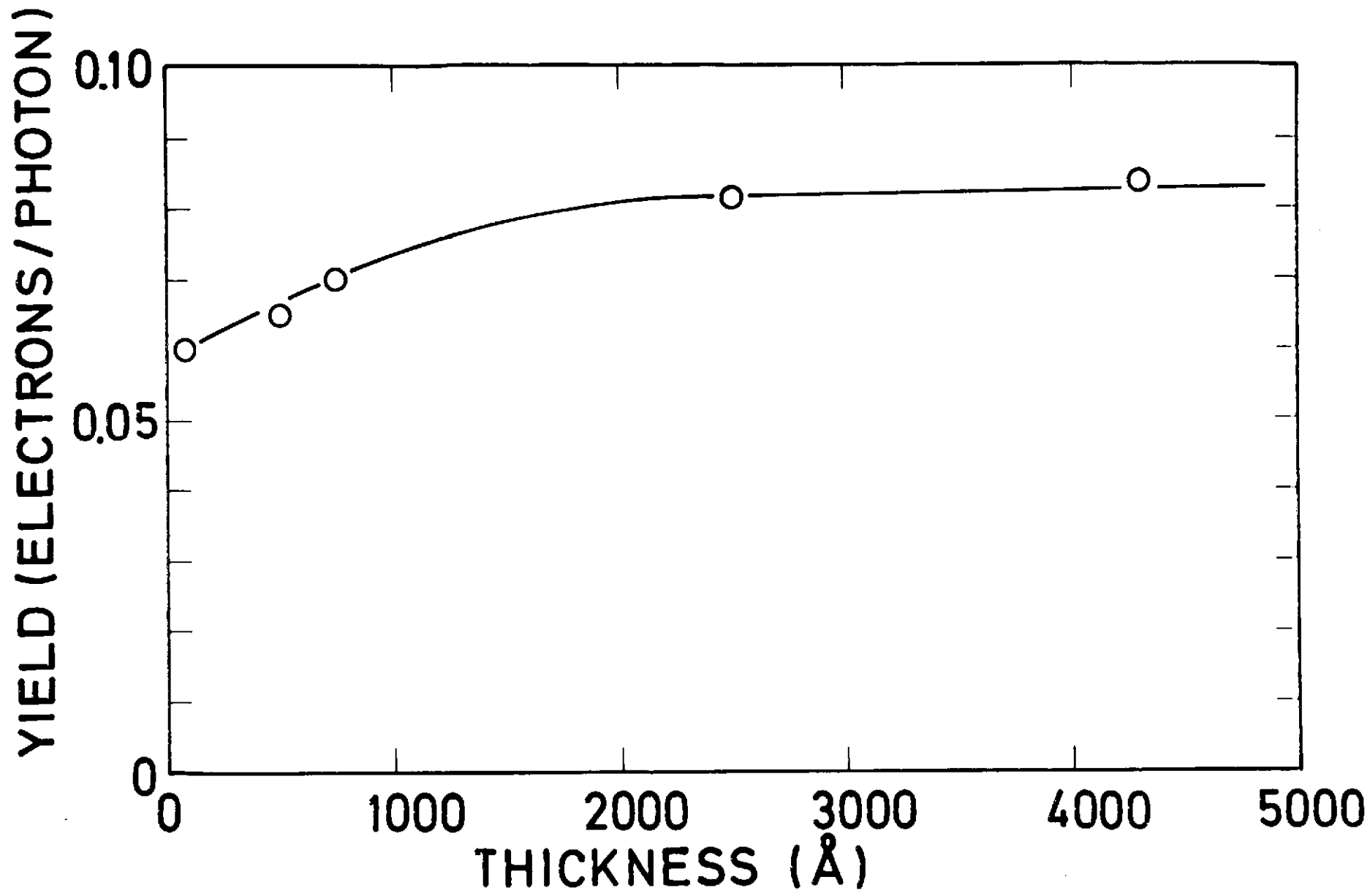


FIG. 6

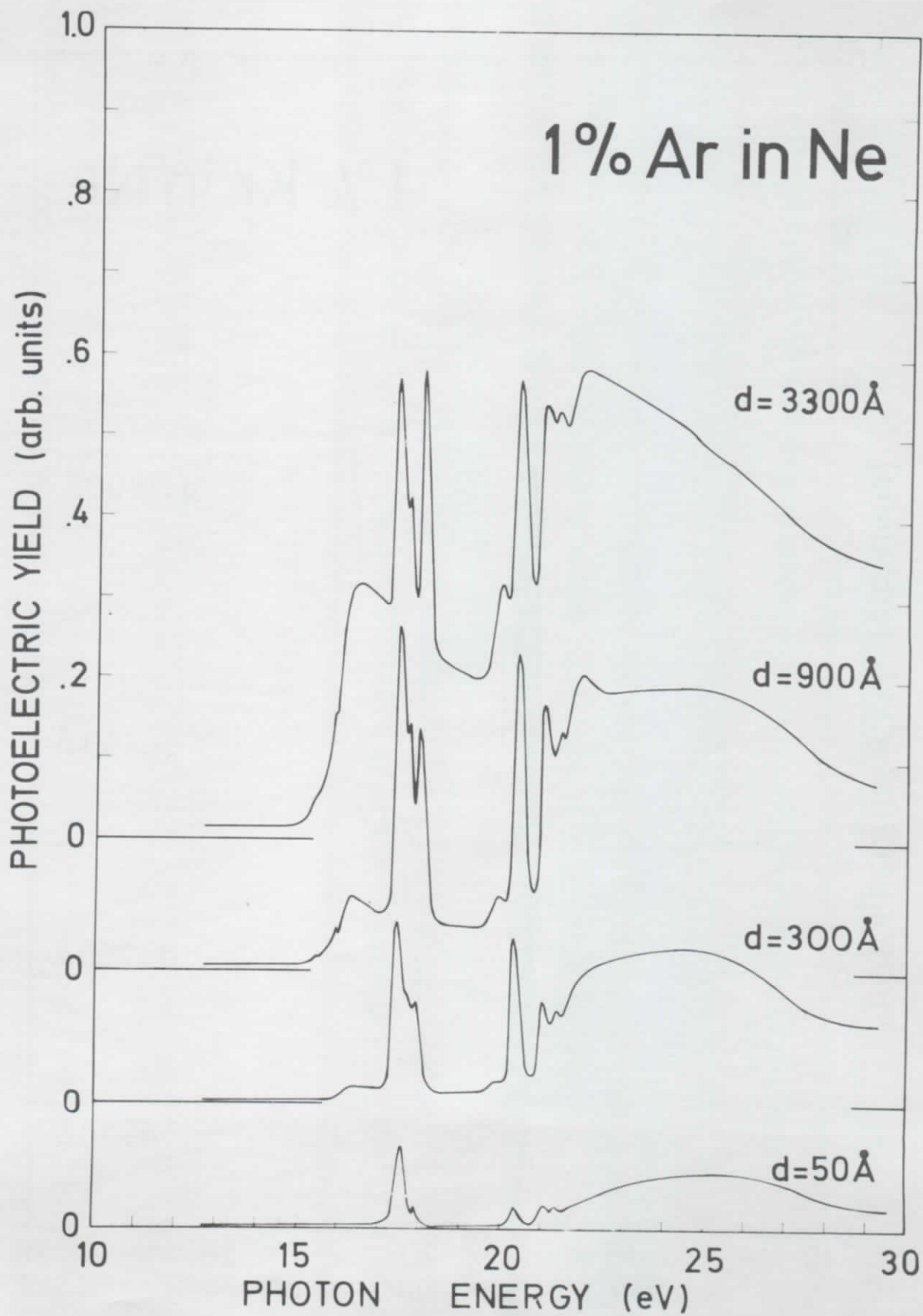


Fig. 7

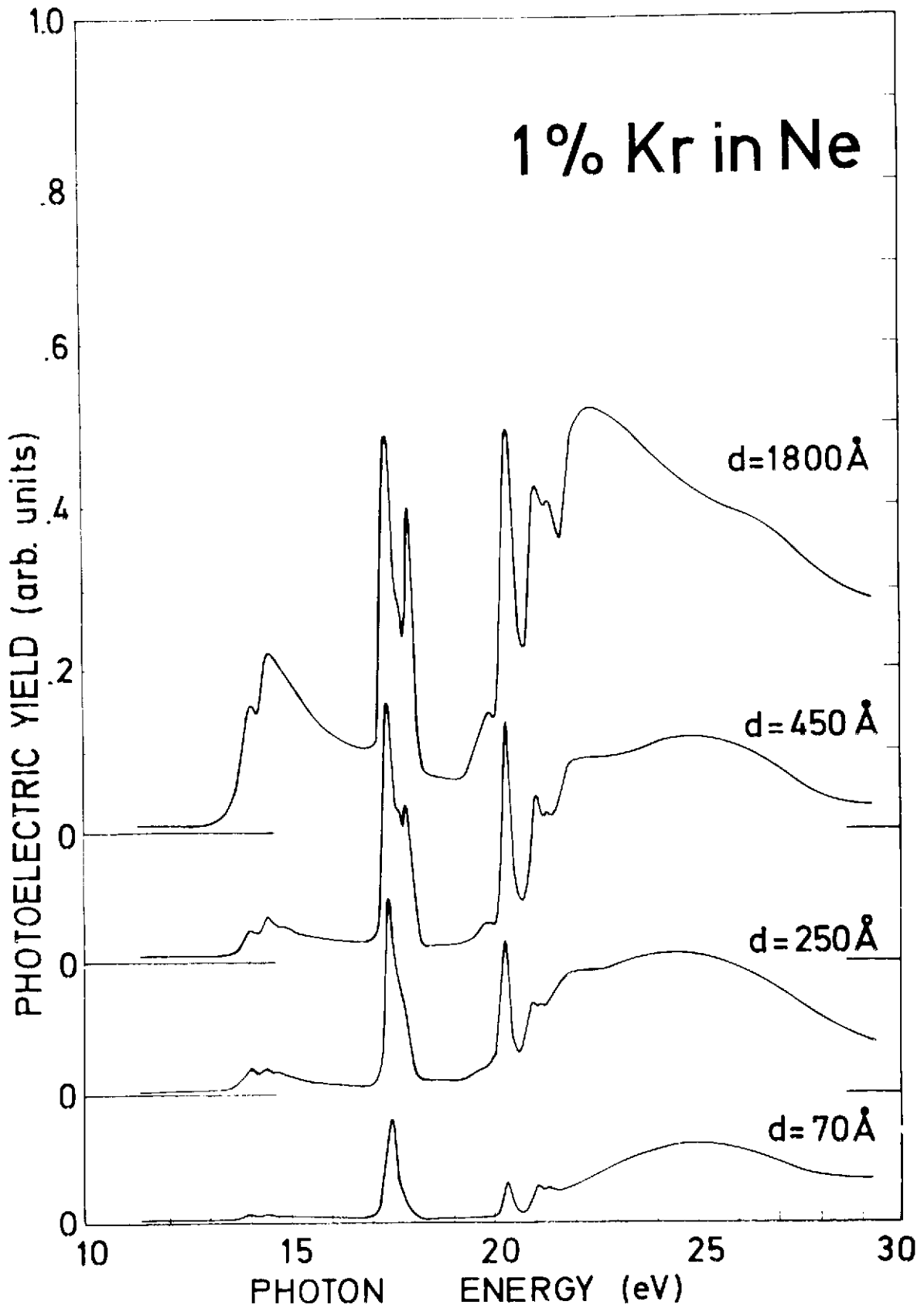


FIG. 8

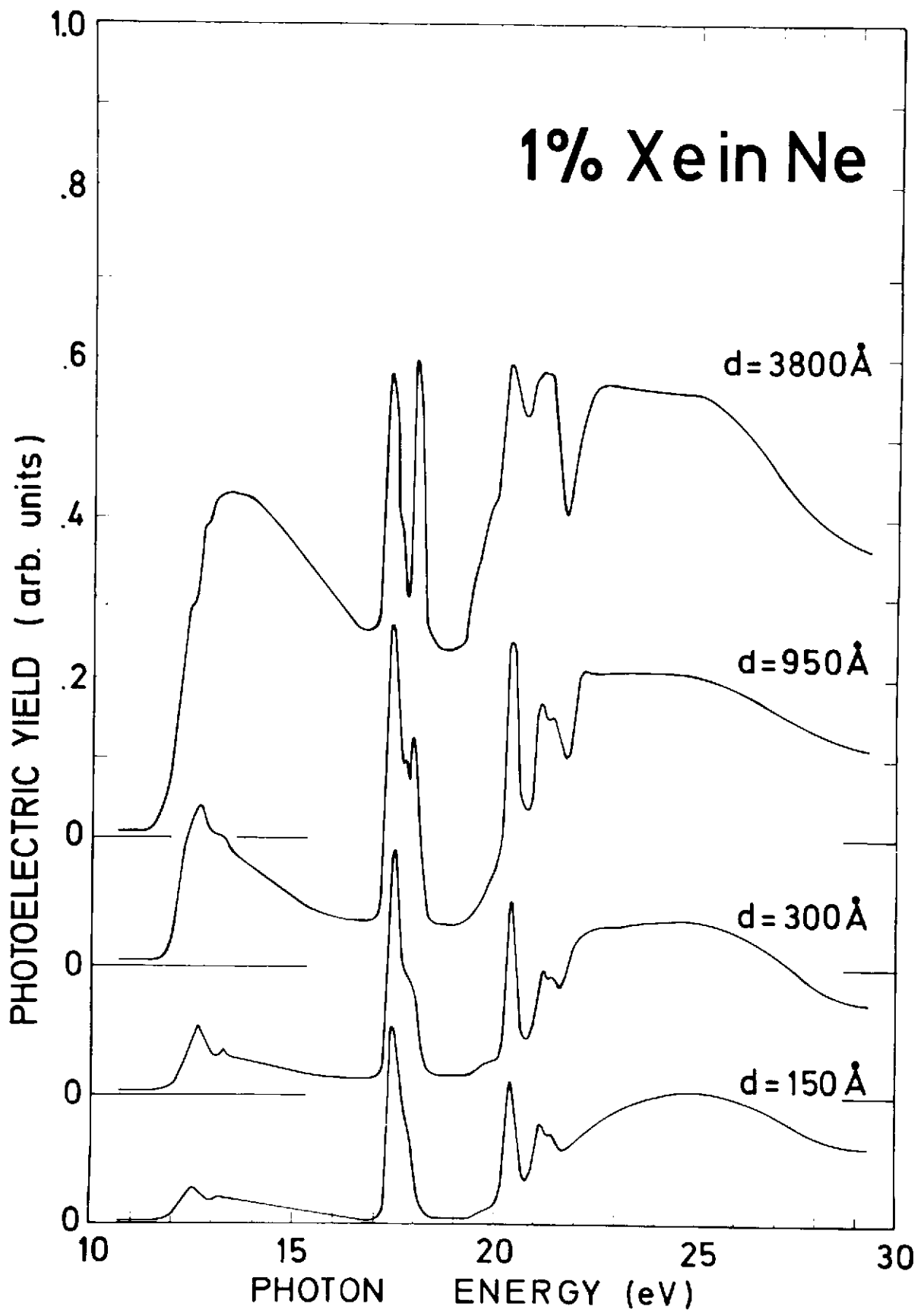


Fig. 9

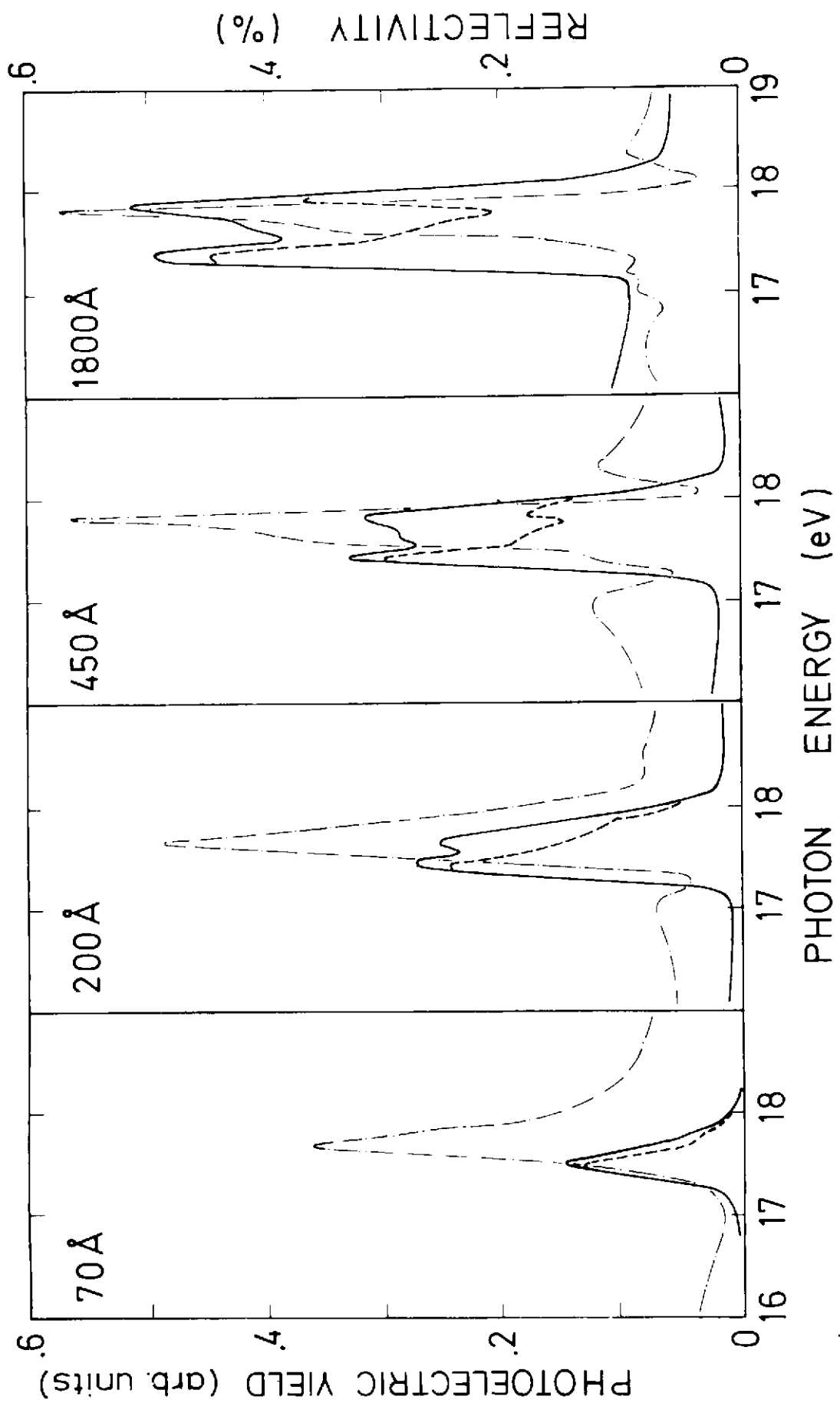


FIG. 10

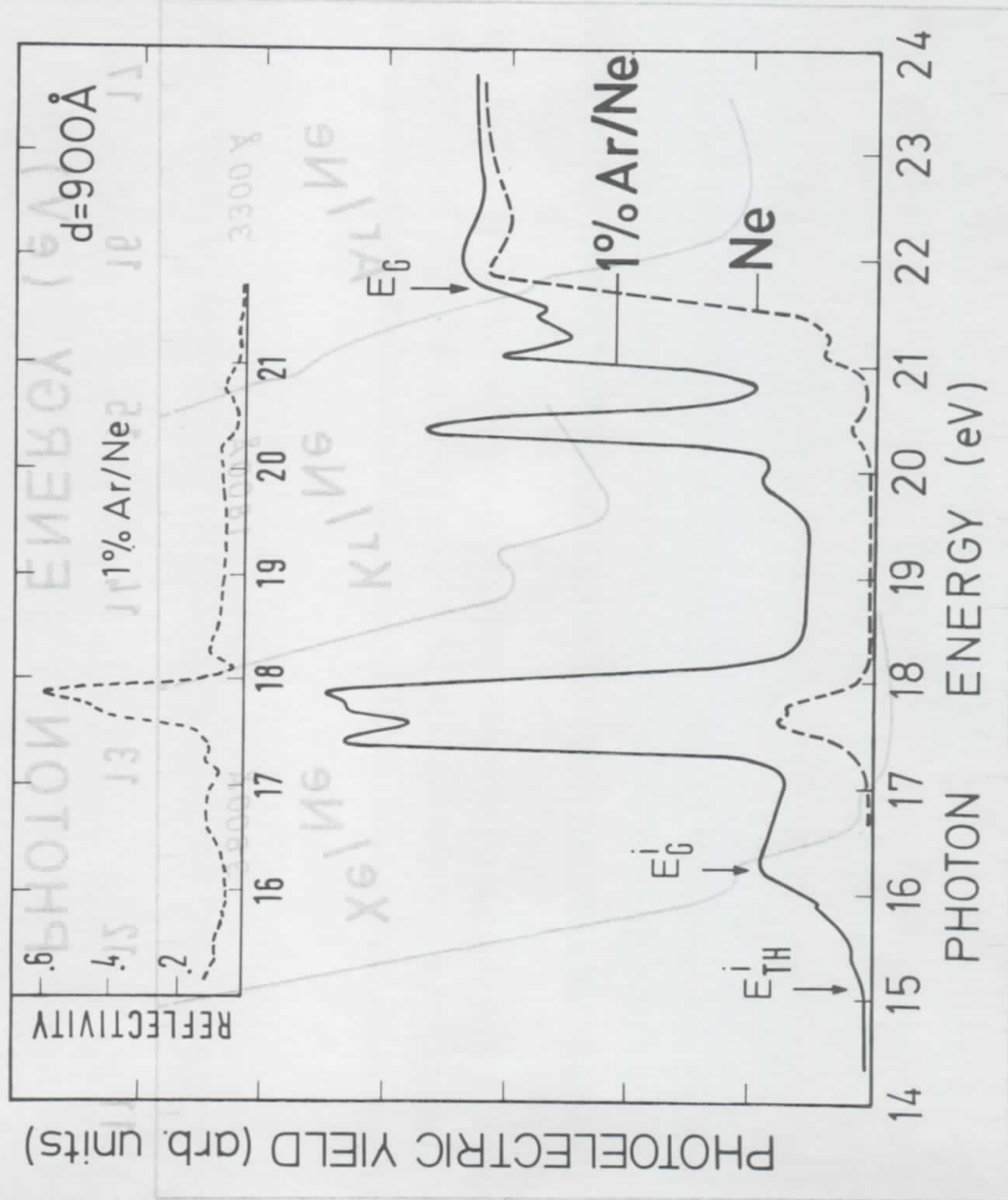


FIG. 11

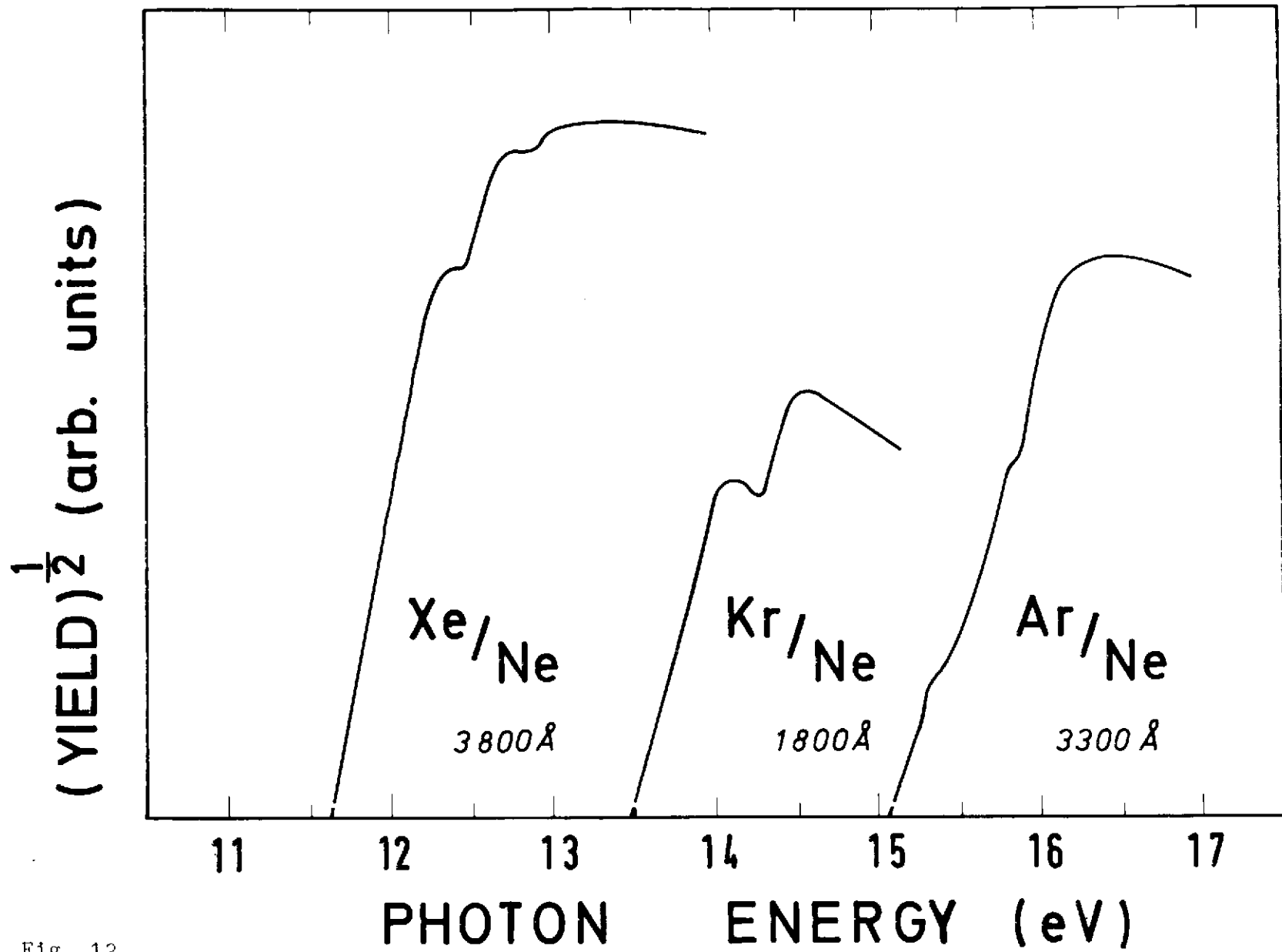
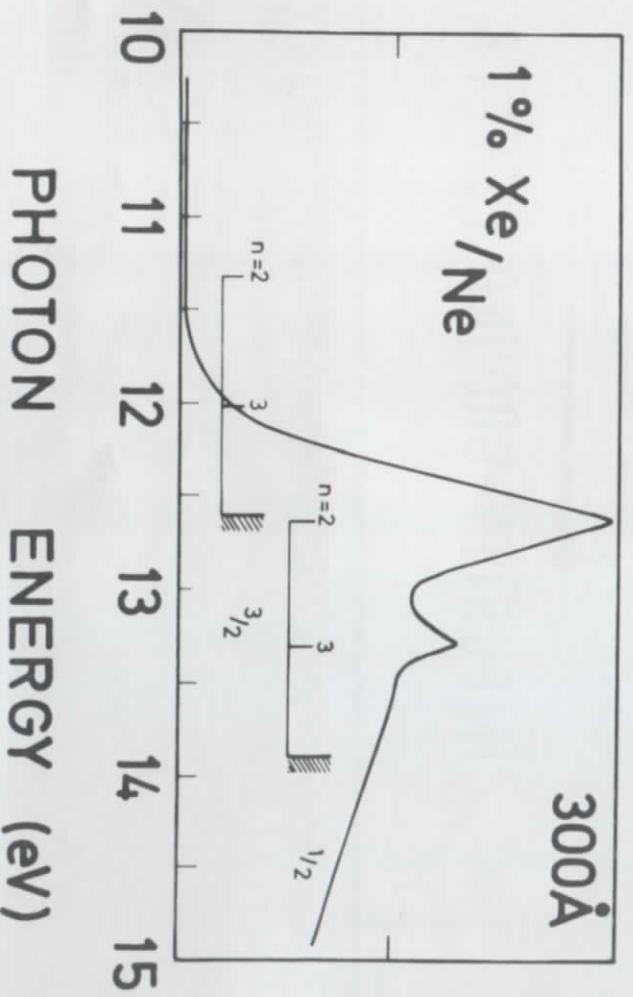
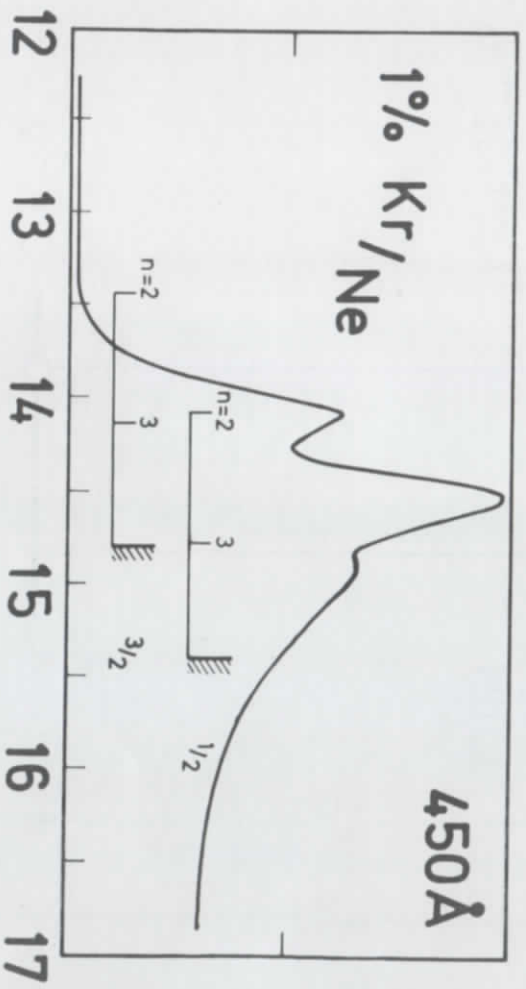
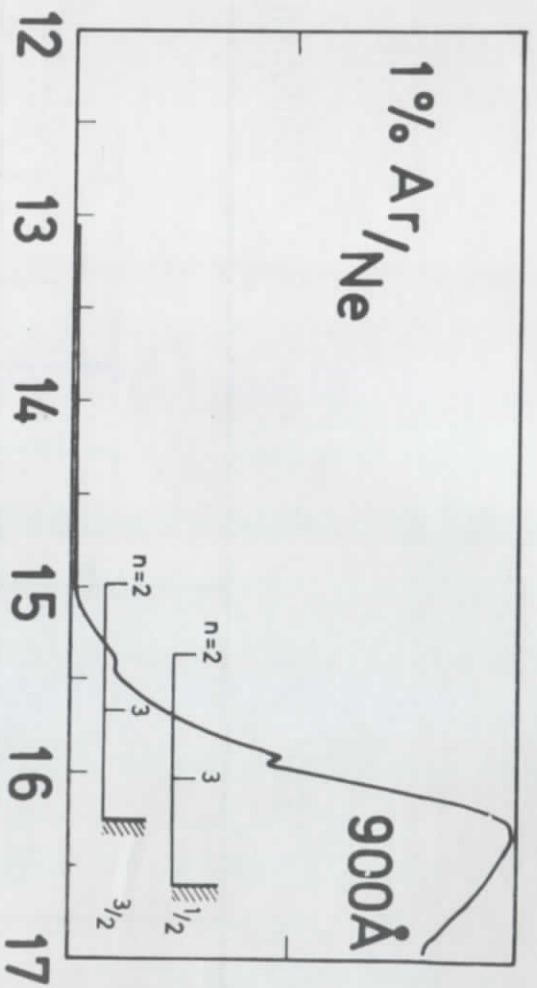


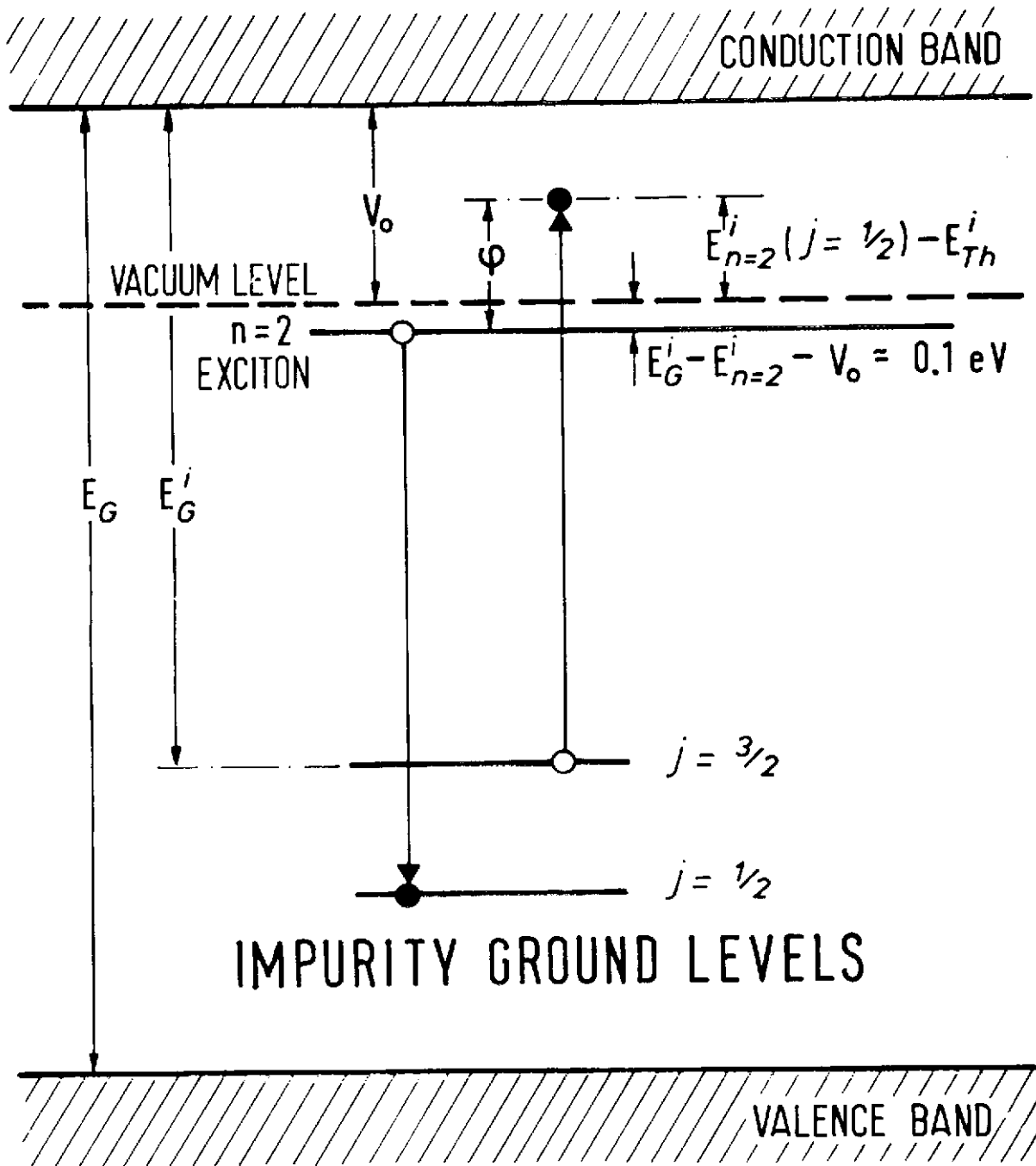
Fig. 12

PHOTOELECTRIC YIELD (arb. units)



PHOTON ENERGY (eV)

FIG. 13



Ne

Fig. 14

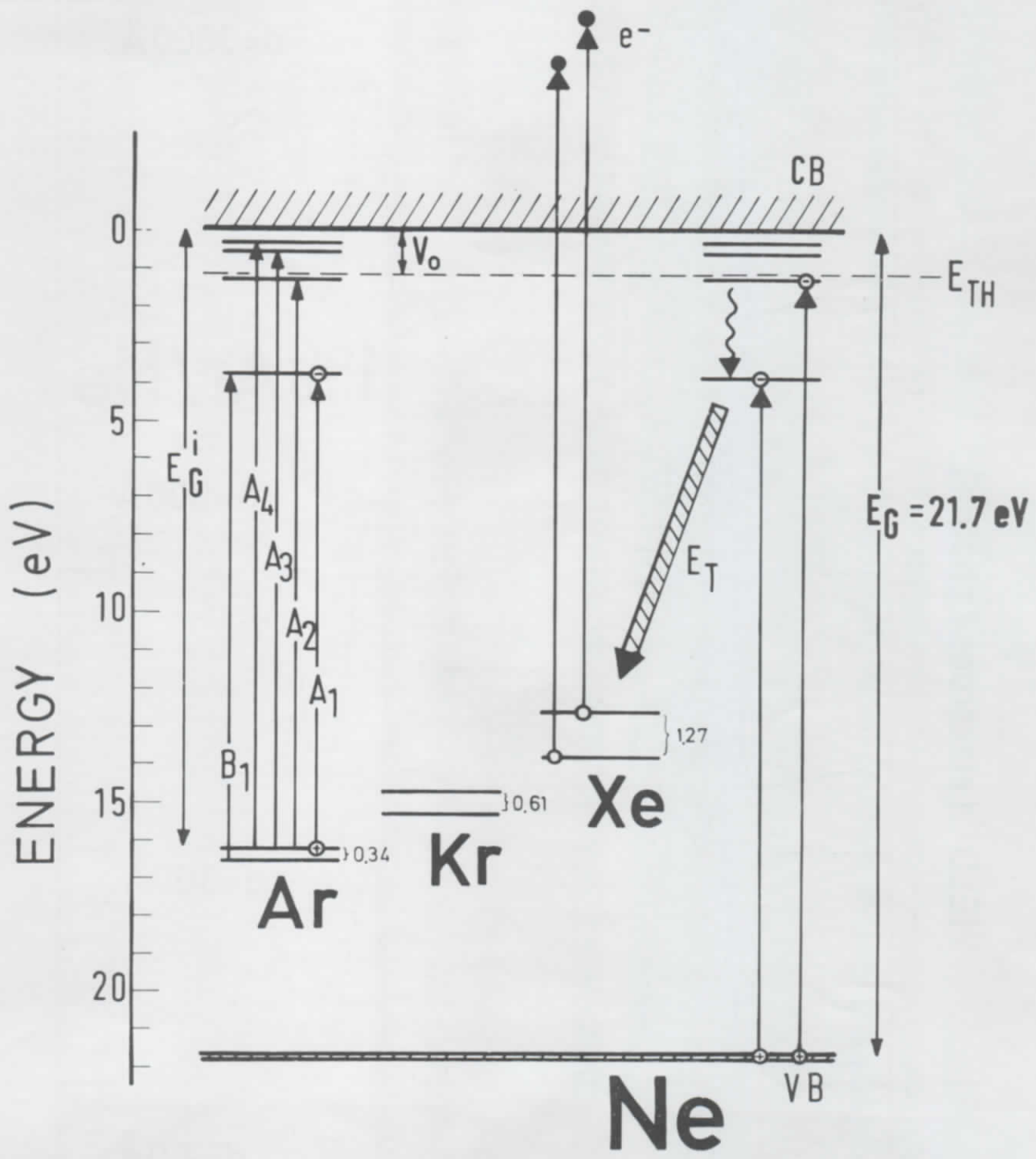


Fig. 15

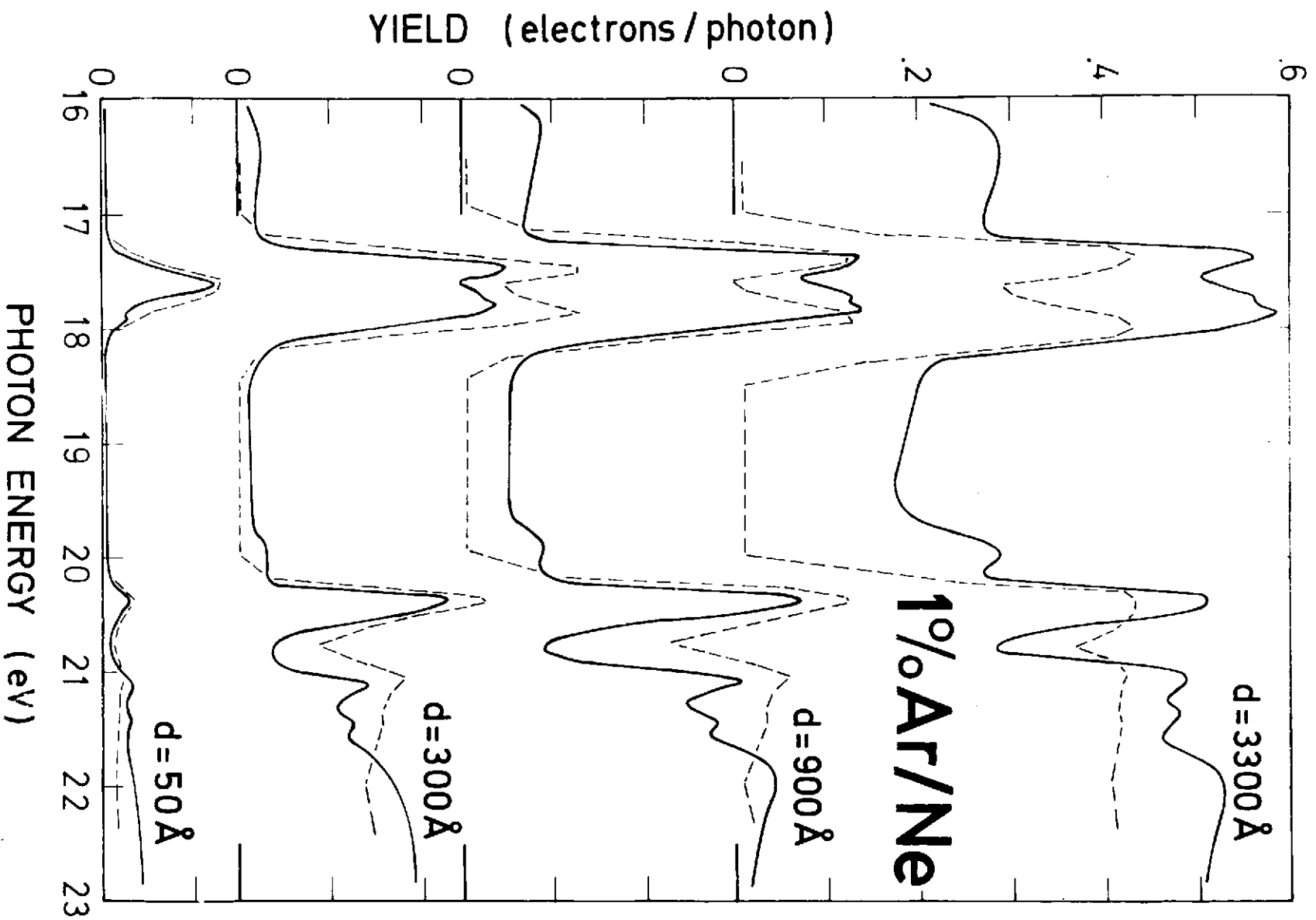


FIG. 16

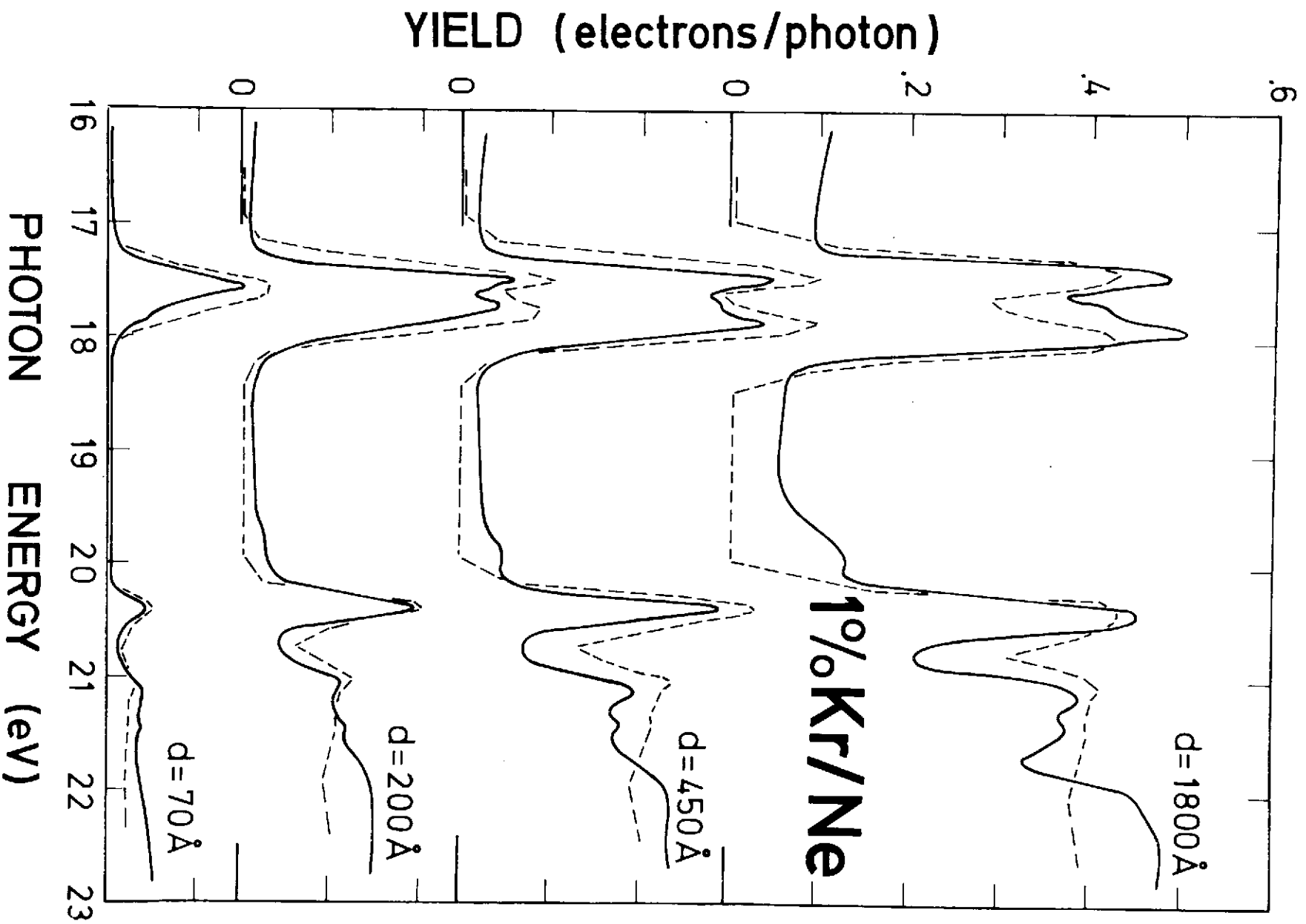


FIG. 17

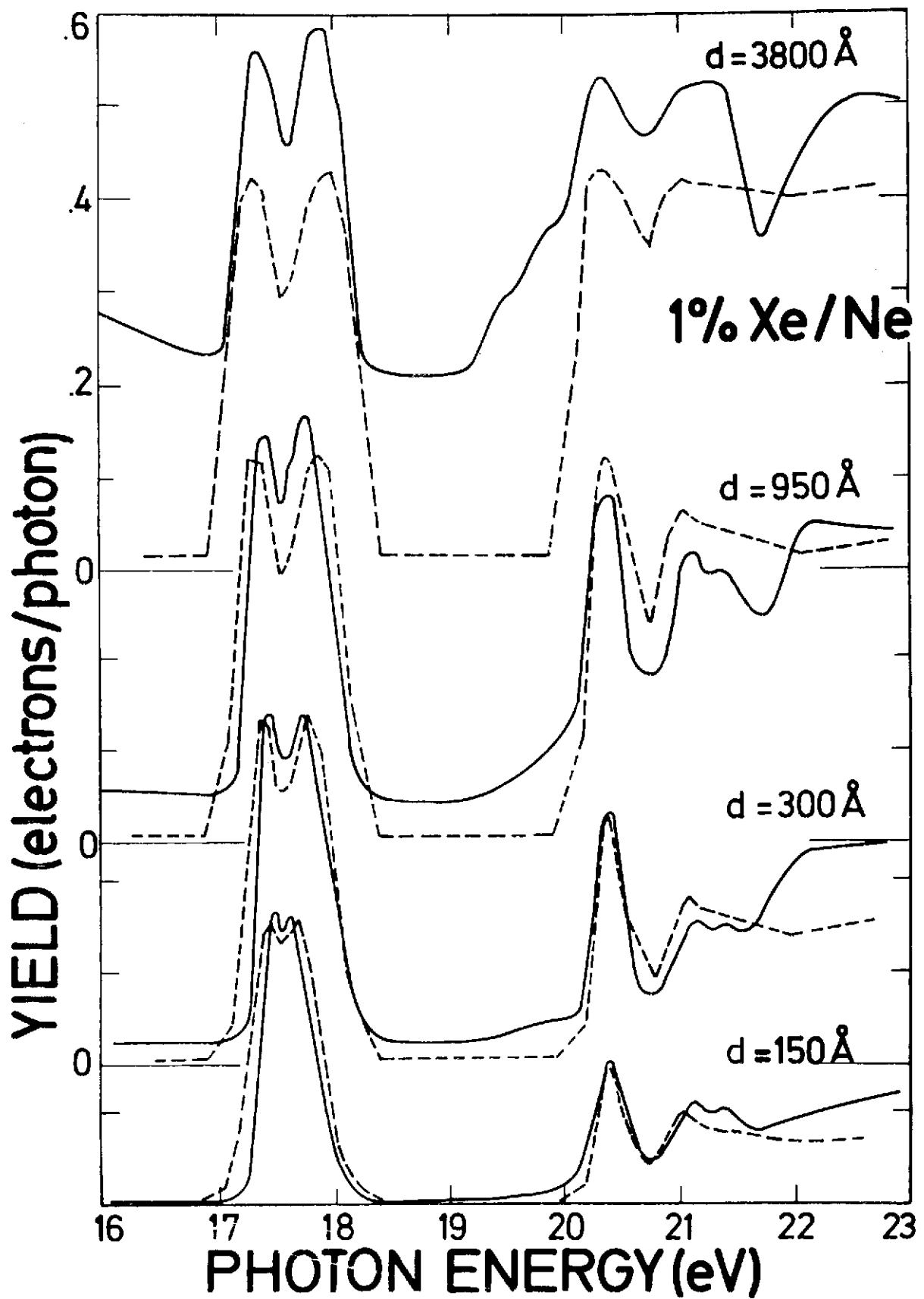


Fig. 18

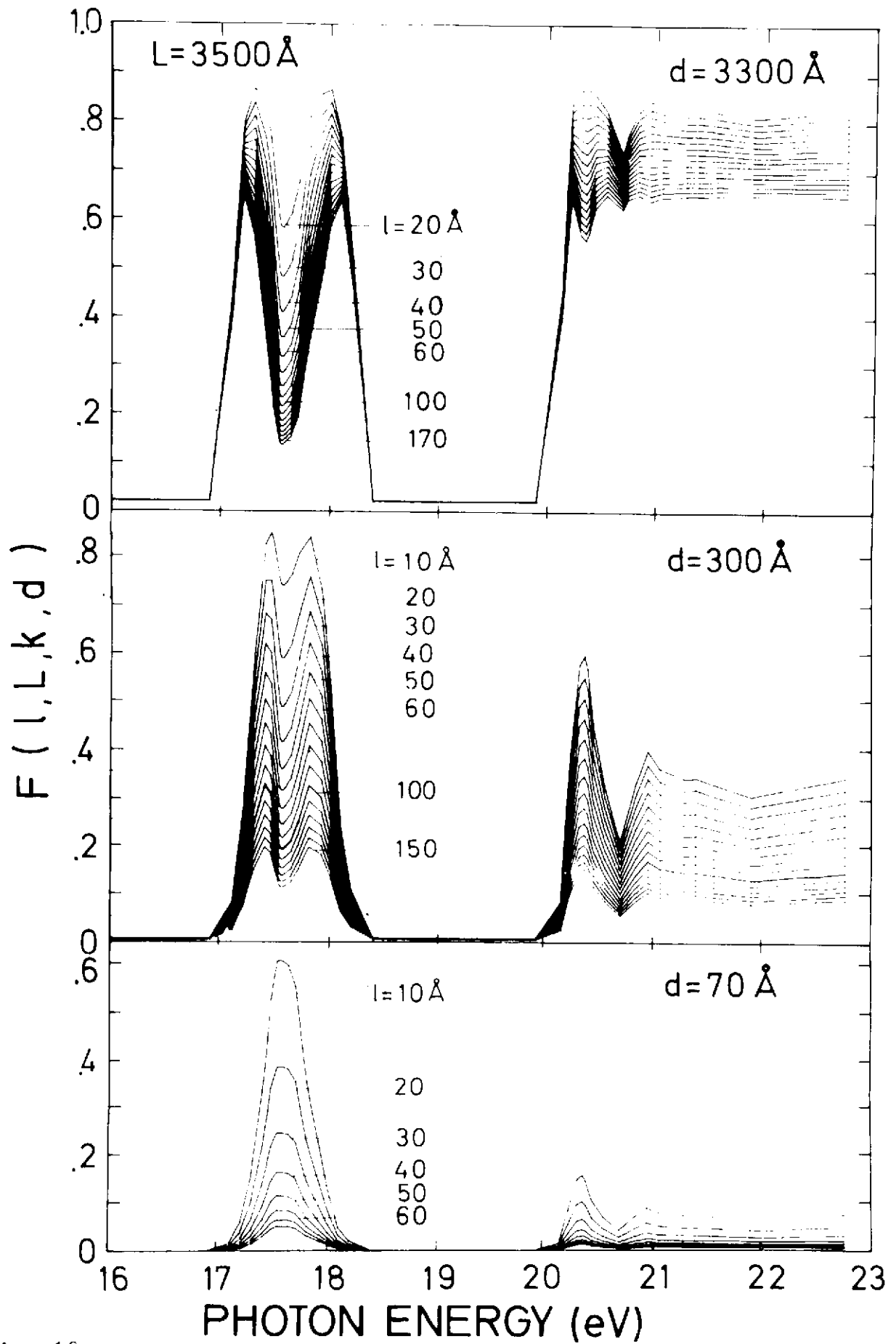


Fig. 19

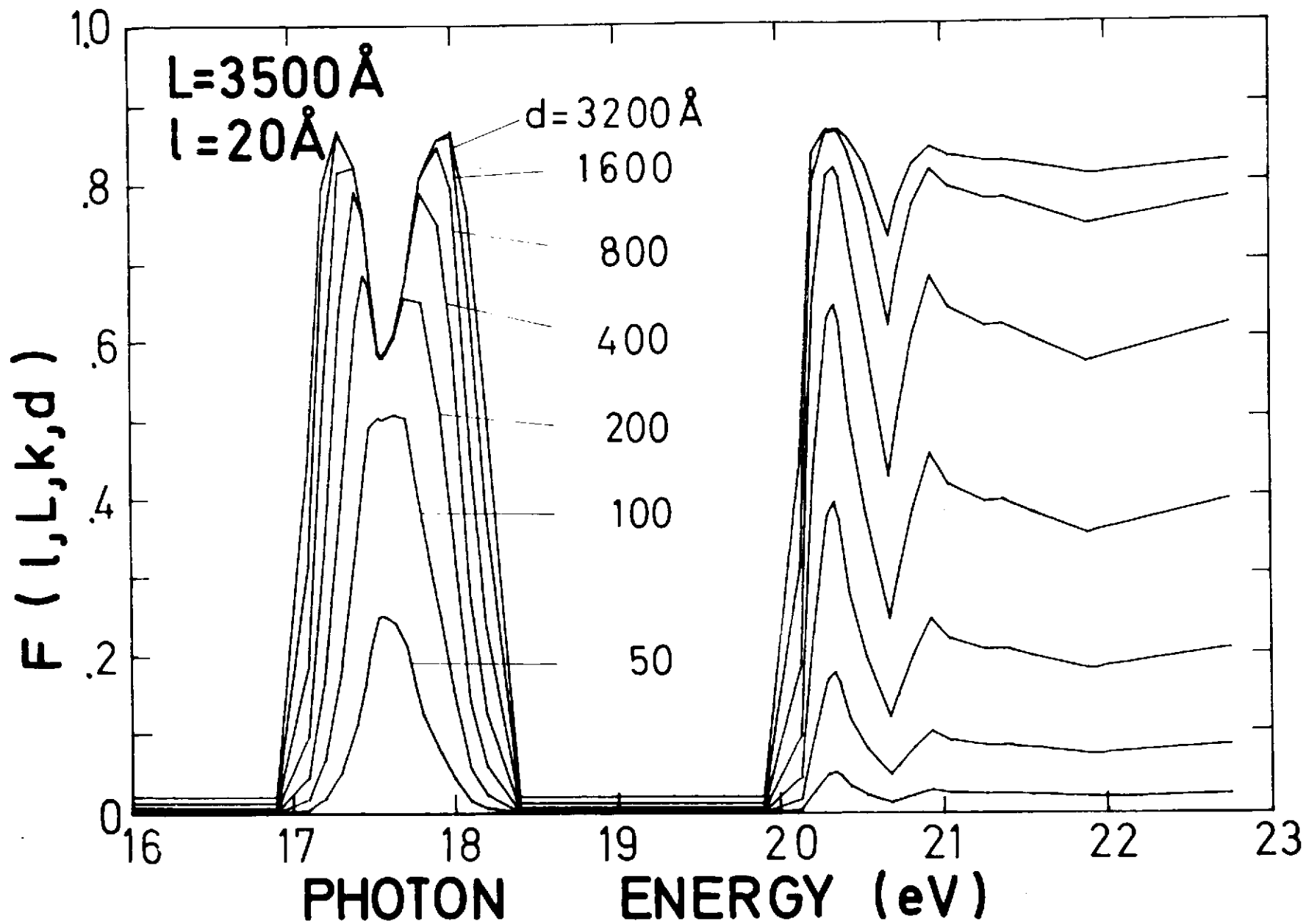


Fig. 20

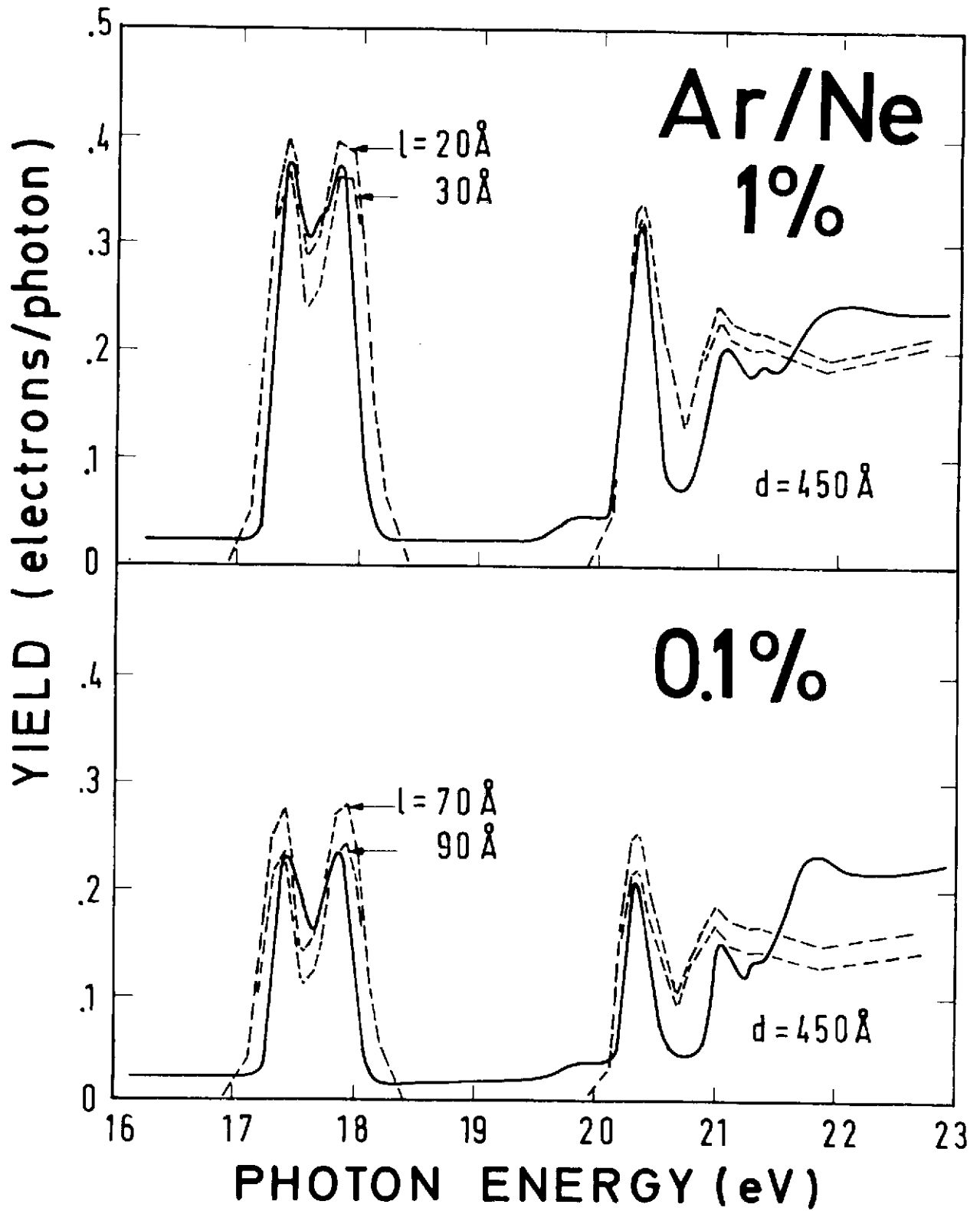


Fig. 21

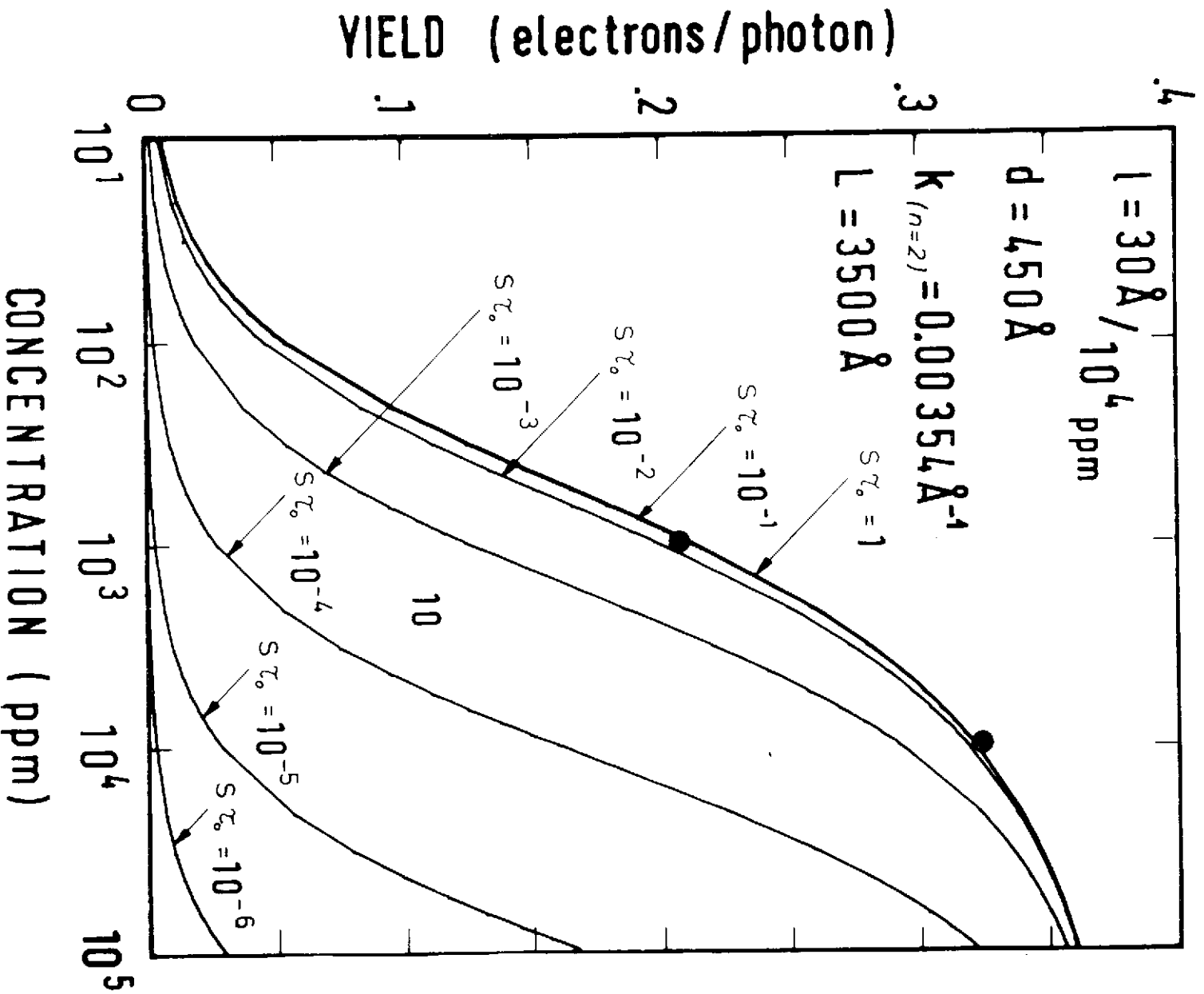


FIG. 22